IOP Publishing Mater. Quantum Technol. 4 (2024) 012001 https://doi.org/10.1088/2633-4356/ad2980

Materials for Quantum Technology

OPEN ACCESS

RECEIVED
17 July 2023

REVISED
5 December 2023

ACCEPTED FOR PUBLICATION
14 February 2024

PUBLISHED
26 February 2024

TOPICAL REVIEW

Recent progress in undoped group-IV heterostructures for quantum technologies

Chia-Tse Tai[1,5] and Jiun-Yun Li[1,2,3,4,*]

[1] Graduate Institute of Electronics Engineering, National Taiwan University, Taipei 10617, Taiwan
[2] Department of Electrical Engineering, National Taiwan University, Taipei 10617, Taiwan
[3] Graduate School of Advanced Technology, National Taiwan University, Taipei 10617, Taiwan
[4] Taiwan Semiconductor Research Institute, Hsin-Chu 30078, Taiwan
[5] Current address: Department of Electrical and Computer Engineering, Princeton University, Princeton, NJ, United States of America.
[*] Author to whom any correspondence should be addressed.

E-mail: jiunyun@ntu.edu.tw

Keywords: spin-orbit coupling, effective mass, surface tunneling, mangeto-transport properties, two-dimensional electron/hole gas, quantum technologies, g-factors

Abstract

Silicon has been a core material for digital computing owing to its high mobility, stability oxide interface, mature manufacturing technologies for more than half a century. While Moore's law seems to further advance via various technologies to extend its expiration date, some intractable problems that requires processing times growing exponentially cannot be solved in a reasonable scale of time. Meanwhile, quantum computing is a promising tool to perform calculations much more efficiently than classical computing for certain types of problems. To realize a practical quantum computer, quantum dots on group-IV semiconductor heterostructures are promising due to the long decoherence time, scalability, and compatibility with the Si very-large-scale integrated technology. In this review, we start with the advancement of group-IV undoped heterostructures since 2000 and review carrier transport properties in these undoped heterostructure. We also review the hole effective masses, spin-orbit coupling, and effective g-factors in the Ge-based heterostructures and conclude with a brief summary.

1. Introduction

Moore's law has been successful to drive the development of very-large-scale integrated (VLSI) circuits for more than six decades, enabling high-performance computing (HPC), artificial intelligence (AI), edge computing, and in-memory computing for the coming decades. While HPC and AI are expected to further lead us to an unprecedented scenario, the requirement of big-data processing, cryptography, and drug discovery might post an insurmountable barrier for classical computers. In 1994, Shor proposed a quantum algorithm using the quantum properties, such as superposition and entanglement, to solve intractable problems by classical computing [1]. Since then, many platforms to realize quantum bits (qubits) have been demonstrated, such as superconductors [2], ion traps [3], nitrogen-vacancy centers [4], and semiconductors [5]. Among them, semiconductor qubits have attracted a lot of attention due to the long decoherence time, scalability, and compatibility with mature VLSI technologies. In 2005, Petta *et al* demonstrate coherent control of electrons in a GaAs/AlGaAs-based quantum dot (QD) [5]. While this heterostructure has the highest carrier mobility (up to 4.4×10^7 cm^2 (V s)$^{-1}$ [6]), the non-zero nuclear spins in GaAs results in a much shorter coherence time than Si (∼10 ms [7]). The nuclear spin (I) in GaAs is $I = 3/2$ (The Ga isotope, ^{69}Ga and ^{71}Ga, and ^{75}As all have $I = 3/2$ [8]. On the other hand, among the three most common isotopes found in natural Si, only ^{29}Si has non-zero nuclear spin $I = 1/2$ [8], which couples to the electron spin through the hyper-fine interaction and causes dephasing [9]. Si is a promising material for spin-based quantum computing due to its relatively low amount of nuclear spins to suppress spin decoherence of electrons. This can be achieved by isotopically enrichment of ^{28}Si, reducing the fraction of ^{29}Si [10]. In 2012, an ultra-long coherence lifetime up to 2 s was achieved in a highly purified ^{28}Si material (residual ^{29}Si

<50 ppm) [10]. The focus has been turned to the Si QD devices and in 2012, coherent control of electron spins in Si QDs was demonstrated [11] and high fidelity >99.9% in a Si MOSFET [12] or a Si/SiGe heterostructure [13] was presented. In 2022, a six-qubit QD array by top gating was demonstrated on an undoped Si/SiGe heterostructure [14]. In addition to Si-based qubits, Ge-based qubits have recently attracted a lot of attention due to the strong spin-orbit coupling (SOC). In 2020, a fast two-qubit operation was achieved in a gated QD on an undoped Ge/GeSi heterostructure [15]. A four-qubit device on a Ge/GeSi heterostructure was demonstrated in 2021 [16]. While the development of semiconductor qubits is still in its infancy, the mature semiconductor manufacturing technology and the ecosystems are the strongest support for the promises of the semiconductor qubits.

To fabricate an electrostatically defined QD in an undoped system, a two-dimensional electron gas (2DEG) or a two-dimensional hole gas (2DHG) is firstly formed in the semiconductor heterostructures. In Si/SiGe or Ge/GeSi heterostructures, the SiGe or GeSi layer must be strain-relaxed to provide the required energy offset in the conduction band or valence band between the Si/SiGe or Ge/GeSi heterointerface, respectively [17]. Since there is a large lattice mismatch between Si and Ge, the strain relaxation in the group-IV heterostructures leads to a very rough surface [18] and a high density of dislocation defects [19]. Thus, the typical carrier mobility in group-IV heterostructures is one to two orders of magnitude smaller than that in the GaAs system. Mobility is a fundamental physical parameter for carrier transport and often used to evaluate the impact of disorder. A higher mobility means a longer mean free path of carriers and less disorder. To observe quantum Hall effects in 2DEG or 2DHG systems, a high carrier mobility is required. For a large-scale qubit, less disorder is also required for fault-tolerant quantum computing. Thus, in this work, we will briefly review the carrier mobility in undoped group-IV heterostructures. Moreover, severe surface segregation of n-type dopants in the group-IV materials results in significant gate leakage [20], which further prevents development of gated structures for QD applications. To solve this issue, an undoped heterostructure is the solution owing to the absence of the n-type dopants. In 2009, an extremely high electron mobility of $\sim$1600 000 cm^2 (V s)$^{-1}$ was demonstrated in the undoped Si/SiGe heterostructure [21]. Since many nano-lithographic steps for very precise alignments and subsequent atomic layer deposition (ALD) of multiple dielectric layers are required for the QD fabrication, the surface roughness of the wafers is critical and could further hamper yields of device fabrication. The rough surface can be remedied by combining chemical mechanical polishing (CMP) and re-growth techniques. An ultra-flat undoped Si/SiGe heterostructure with a mobility of $\sim$160 000 cm^2 (V s)$^{-1}$ and quantum Hall plateaus and Shubnikov-de Haas (SdH) oscillations was demonstrated using CMP and commercial epitaxy tools, such as chemical vapor deposition (CVD) [22]. While the polishing step does reduce the surface roughness, in-situ baking to clean wafer surfaces before the regrowth steps is only allowed at low temperatures to avoid the dislocation and material defects created during a conventional high-temperature cleaning step. Thus, more impurities might be introduced into the Si/SiGe heterostructure, leading to a much reduced mobility (16 000 cm^2 (V s)$^{-1}$).

In 2017, high hole mobility ($\sim$200 000 cm^2 (V s)$^{-1}$) in an undoped Ge/GeSi heterostructure was demonstrated [23], enabling the Ge-based qubit development utilizing its strong SOC effects [24–26]. The SOC effects in Ge originates from the relativistic interaction of holes' spin with their motion in electric potentials created by the nuclei. Under the Lorentz transformation, the hole spin couples to a $\vec{k}$-dependent effective electric field. The SOC plays an important role in spintronics [27] and spin-based quantum computing [15, 16, 28, 29] as it provides an effective way to control spin states through electrical gating. A 2DHG in the Ge-based heterostructure is a promising platform because of it strong SOC effect and compatibility with the VLSI technology. A fast two-qubit gate reached a Rabi frequency exceeding 100 MHz in 2020 [15]. In 2021, Tai *et al* demonstrated even larger SOC strengths in GeSn [30] than in Ge [26]. With its direct-bandgap characteristics [31] and high carrier mobility [32, 33], GeSn is a promising enabler to accomplish a full-functional chip including spintronic, photonic, and electronic devices compatible with the Si CMOS platform.

The effective mass (m^*) and effective g-factor (g^*) are key materials parameters for the response of carrier transport to electric fields and magnetic fields, respectively. While both parameters are well known in bulk Ge, they deviated from the bulk values in a QW structure [34, 35] or under stresses [36]. For example, reduction of effective mass in strained Ge was demonstrated both theoretically [37] and experimentally [36]. A small effective mass is desired for high-performance electronic devices owing to the enhanced mobility. Furthermore, for QD applications, a smaller effective mass enables stronger qubit entanglement due to the more spread wavefunctions and allows larger dimensions in the QD devices, alleviating the complexity of nano-fabrication processes [15]. The g-factors directly links to the Zeeman splitting energy, which is important for the spin readout [38], initialization [39], and manipulation [40]. The tunability of g-factors [41] or anisotropy [35] in Ge attracts much attention as a larger g^* effectively reduces the associated magnetic field for the required Zeeman splitting in a spin qubit [42].

For the extensive reviews on the Ge-based spin qubits, one can consult [43, 44]. While the spin-based properties, such as SOC or g-factors, were reviewed in theoretical perspectives in those reports, there is not much focus on the experimental results of quantum transport in undoped group-IV heterostructures. In this review, we start with the introduction to the physics of undoped group-IV heterostructures, such as Si/SiGe, Ge/GeSi and GeSn/Ge heterostructures. We will briefly introduce the carrier transport and discuss the scattering mechanisms in those undoped heterostructures. Moreover, we discuss the unique properties of surface tunneling of carriers in the buried channel in the undoped heterostructure. Then we discuss experimental results of hole effective mass, SOC effects, and g-factors in the Ge-based heterostructures. Last, we conclude by providing our perspectives on future directions.

2. Characteristics of group-IV heterostructures

2.1. Si/SiGe heterostructures

In 80's and 90's, 2DEGs on the modulation-doped heterostructures, such as GaAs/AlGaAs [45], Si/SiGe [46], etc. were extensively investigated. A lot of exciting physics had been explored and some of them have become very powerful metrology or foundation for useful applications, such as quantum computation [14, 47, 48] and spintronics [49, 50]. In 2005, coherence control of spins was demonstrated using a modulation-doped GaAs/AlGaAs heterostructure [5] owing to its excellent material quality. However, its non-zero nuclear spin limits spin manipulation within a very short period via the hyperfine interaction. Since the zero nuclear spin in ^{28}Si isotope results in no hyperfine interaction, the spin decoherence can be effectively suppressed by the enrichment of ^{28}Si isotope [51]. An extremely long coherence time of $\sim$2 s is reported in [10]. Researchers have turned their focus into Si-based quantum computing since 2010. While the initial effort was on making QDs on the modulation-doped Si/SiGe heterostructures, little progress was made due to the issues of gate leakage, ineffective gate control over the buried 2DEG [52], or dopant fluctuation [53].

The first modulated-doped Si/SiGe heterostructure was epitaxially grown by molecular beam epitaxy (MBE) [54] and an extremely high mobility up to 800 000 cm^2 (V s)$^{-1}$ was demonstrated [55]. However, the low yield and non-equilibrium growth mode could possibly lead to a higher defect density in epitaxial layers. On the other hand, CVD, a commercially available tool with high throughputs, has been used to grow high-quality group-IV heterostructures, such as Si/SiGe [21, 56], Ge/GeSi [23, 57, 58], and GeSn/Ge [30]. In 2009, Lu *et al* demonstrated an extremely high electron mobility of 1600 000 cm^2 (V s)$^{-1}$ on an undoped Si/SiGe heterostructure by ultra-high vacuum CVD (UHVCVD) [21]. Gate control over the 2DEG is clearly presented without any gate leakage using a metal-oxide gate stack. Without using a remote doping layer to modulate the carrier density, 2DEG in an undoped structure is controlled by the top gate. Figure 1 shows the band diagrams of both a modulated-doped and an undoped Si/SiGe heterostructures. In figure 1(a), there exists an energy minimum in the SiGe layer due to the carrier diffusion. The carrier density is modulated by the doping concentration and the distance between the doped layer and the Si quantum well. There are few main issues for the modulated-doped structure. First, unlike the GaAs/AlGaAs structure, where the technique of the deposition of a delta-doped layer is well developed, for Si-based structure, the n-type dopants tend to segregate to the surface [20], leading to a higher concentration at the surface and thus, the serious gate leakage. The high phosphorus concentration leads to a rougher surface and dopant fluctuations, leading to a further reduced carrier mobility [53]. Lowering the growth temperature during the epitaxial processes could effectively suppress the surface segregation of n-type dopants in group-IV materials [20] and effective Schottky gating was demonstrated using palladium as the gate metal [59]. An extremely high mobility of 522 000 cm^2 (V·s)$^{-1}$ was reported in ^{28}Si-enriched modulated-doped heterostructure with an ultra-low carrier density of $\sim 8 \times 10^{10}$ cm^{-2} by top gating to effectively deplete the carriers in the 2DEG layer [60].

For quantum computing applications, the carrier density should be as low as possible to alleviate the required minimum feature size of the QD devices. While the carrier density can be reduced by increasing the spacing between the doped layer and buried 2DEG, it would also deepen the 2DEG layer since a 50 nm layer of the top-cap SiGe layer is usually required to reduce the concentration of n-type dopants at the surface due to the surface segregation. This will further worsen the gate control over the deep buried channel. In the early stage, some work was done using plasma-enhanced CVD (PECVD) to deposit SiN_x or SiO_2 as a dielectric to isolate the gate metal and the modulated-doped Si/SiGe heterostructure [52]. While the gating should be able to deplete the carriers in the channel, the residual carriers in the doped layer must be depleted first before one can achieve effective control over the buried channel. Thus, removing the remotely doped layer became a feasible way to enhance the gate control over the 2DEG. In an undoped Si/SiGe heterostructure, carriers are injected from the reservoir and their population depends on band distributions set by gate biases. In [21], the gate oxide was deposited by ALD, which avoids the plasma damage by PECVD. The lowest density is below 3×10^{10} cm^{-2} with a reasonably high mobility of 60 000 cm^2 (V s)$^{-1}$ and clear integer and fractional quantum Hall plateaus and SdH oscillations observed at 0.3 K.

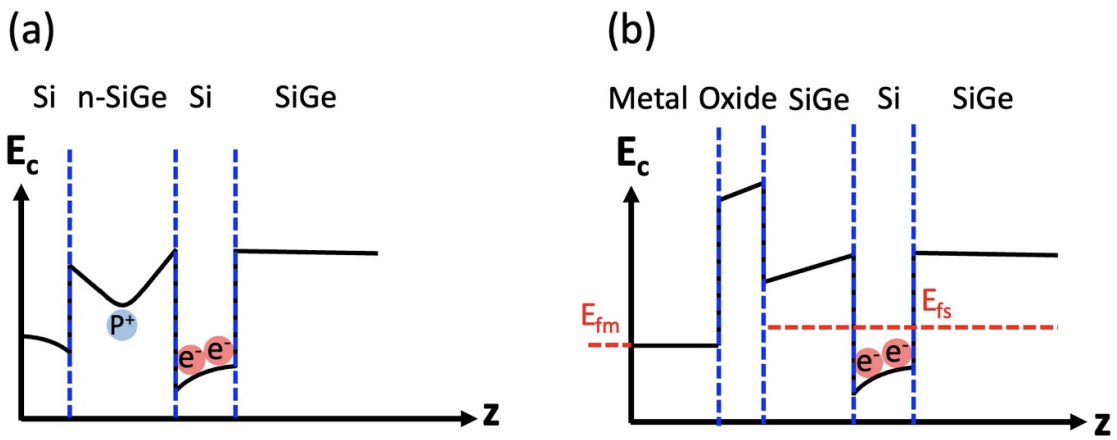

Figure 1. Band diagrams of (a) a modulation-doped and (b) an undoped Si/SiGe heterostructures. E_{fm} and E_{fs} denote the Fermi levels in the metal and semiconductor, respectively.

For the undoped Si/SiGe structure, the highest mobility reported so far is 2400 000 cm^2 $(V\,s)^{-1}$ [61]. The limiting scattering mechanisms were further studied in [62] by increasing the distance between the 2DEG channel and the oxide interface to 526 nm. Similar to the modulation-doped structure, the remote charged impurities at the oxide interface scatter the carriers effectively as the distance between them is short (10–100 nm). In their work, by characterizing the mobility versus density via top gating, they were able to obtain a peak mobility, which was used to investigate the limiting scattering mechanisms. They found that for the undoped Si/SiGe heterostructure with the top SiGe cap layer thicker than 100 nm, the peak mobility stays constants. This indicates the remote impurity scattering from the oxide interface is effectively suppressed. Furthermore, from the μ-n relationship, where n and μ represent the carrier density and mobility of the 2DEG, respectively. A negative dependence was found at a higher carrier density, which is possibly due to alloy scattering or interface roughness scattering [63]. By varying the Ge fraction in the SiGe spacer, they characterized the surface roughness and the threading dislocation density in the Si/SiGe heterostructures with different Ge fractions (figure 2). As the Ge fraction increases, the surface becomes rougher and the threading dislocation density is higher due to the larger lattice mismatch between Si and SiGe. According to their calculation, the threading dislocations was not the dominant factor for the upper limit of the mobility, but the background impurity scattering was the limiting factor. In general, if the background impurity scattering dominates the carrier transport, the power of μ-n relationship should be close to 0.5 [62], which was not clearly extracted and discussed in [63]. Based on their calculation, the estimated background impurity concentration is 2.3×10^{14} cm^{-3}, which is close to the substrate doping level. Using a lower-doped Si wafer might be an option to reduce the background impurity concentration and to further boost the peak mobility.

When the top gating induces carriers into the buried channel, the electron wavefunction spreads more into the SiGe layer as the density increases. This leads to stronger alloy scattering and a reduced mobility [62]. However, this was not considered in [63]. Since both alloy scattering and interface roughness scattering results in a dependence of mobility inversely proportional to density, it is not easy to distinguish both effects. Although the predicted mobility by the alloy scattering was much higher than the experimental results, the Ge segregation into the strained Si layer [64] during the hour-long growth could lead to much reduced mobility.

While for the Si/SiGe heterostructure, mobility can be effectively boosted by increasing the distance between the doped layer (or the oxide interface) and the 2DEG layer, a shorter distance between these two layers is preferrable due to the sharp confinement which enables much better control of electric potentials of 2DEG for QD applications. In [21, 63], the carrier transport was investigated for the 2DEG with a depth larger than 100 nm. Laroche *et al* investigated undoped Si/SiGe heterostructures and the scattering mechanisms with the buried 2DEG ranging from 100 nm to 10 nm away from the oxide interface [65]. As the depth is reduced, the peak mobility decreases, which clearly suggests the impurities at the oxide interface are the dominant scattering source. Figure 3 shows the mobility versus density for the buried 2DEGs with different depths. Another useful parameter to analyze scattering mechanisms is the Dingle ratio, defined as τ_{tr}/τ_q. τ_{tr} is the transport lifetime and τ_q is the quantum lifetime. It is an important index to identify the dominant scattering events ($\sim$1 for large-angle scattering and $\gg$1 for small-angle scattering) [66]. The extracted Dingle ratio increases with the 2DEG depth. Large Dingle ratios of 80 $\sim$ 125 indicate the small-angle scattering (e.g. remote impurity scattering at the oxide interface) is more dominant than the

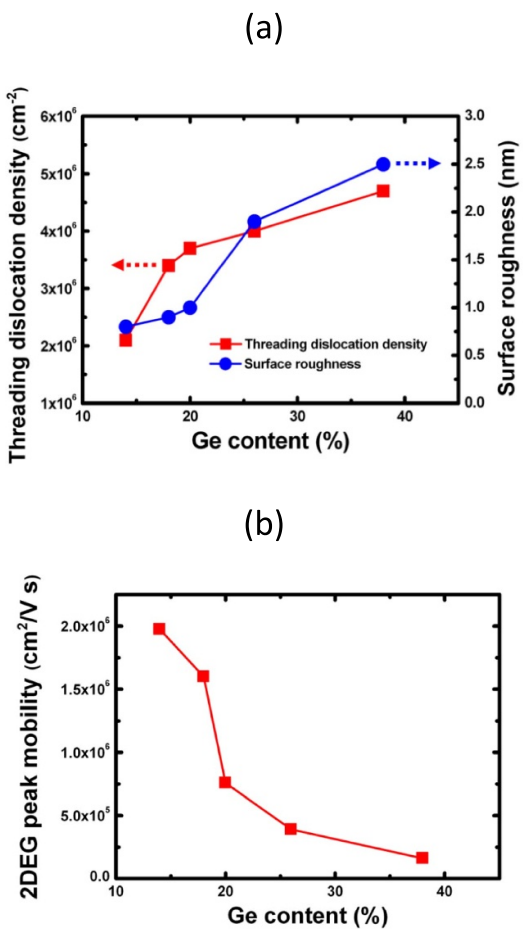

Figure 2. Effects of Ge fraction in a SiGe relaxed buffer on (a) the threading dislocation densities and surface roughness and (b) peak mobility in the 2DEG channel [62]. Reprinted from [62], with the permission of AIP Publishing.

large-angle scattering (e.g. background impurities in the buried quantum well) for the Si/SiGe heterostructure with a much deeper 2DEG. For the shallowest 2DEG, the Dingle ratio is small (∼1.5). A power-law exponent of mobility vs. density was used to further investigate the carrier transport. While the theoretical calculation predicted an exponent of 1.5 for the heterostructures with the depths of 10, 25, and 50 nm limited by the remote impurity scattering, they presented a higher number (∼2.3). By low-density corrections to the random-phase-approximation, this number agrees well with the calculation. However, for the deepest device, the power is 3 and for the 25 nm and 50 nm deep devices, the exponent increases to 5 in a higher-density regime. A non-equilibrium model where trapped electrons smoothen the potential fluctuations at the oxide interface was proposed to explain this high exponent. The authors attributed this non-equilibrium to the surface tunneling of electrons from the buried 2DEG layer to the oxide interface. Since at cryogenic temperatures, the thermal energies of electrons are too low and the surface condition is so severe that electrons at the oxide/Si interface cannot move, increasing the gate bias would not lead to the carriers flowing into the surface channel to reach equilibrium, but to the buried 2DEG layer. By further increasing the gate bias, more electrons are accumulated in the buried channel, resulting in a higher electric field along the vertical direction. Electrons could tunnel to the surface and be trapped at the oxide interface to screen the charged centers at the oxide interface, leading to stronger screening effects on the buried 2DEG and a higher mobility. Monte–Carlo simulations were performed to calculate the density dependence of mobility with a good match with the experimental results.

2.2. Ge/GeSi heterostructures

While the electron transport in the Si/SiGe heterostructures has been well investigated and the high mobility more than 500 000 cm^2 (V s)$^{-1}$ was demonstrated in 90's, the 2DHG had been underdeveloped until an ultrahigh mobility ∼one million was demonstrated in a modulation doped (MOD) system in 2012 [57]. In 90's, 2DHG was formed in a SiGe channel sandwiched by Si layers (figure 4(a)). While this heterostructure with high material quality can be easily grown since a compressive strained SiGe layer can be pseudomorphically grown on a Si substrate without exceeding the critical thickness, the mobility has been

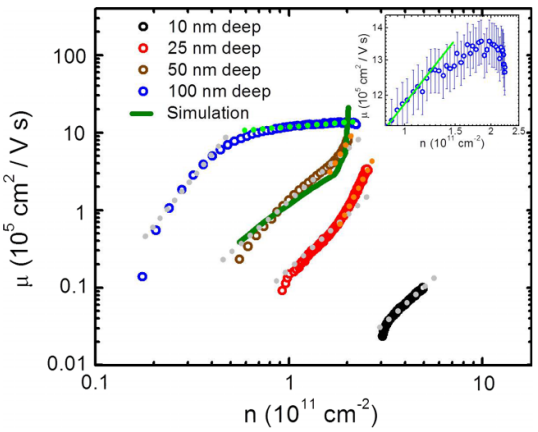

Figure 3. Log–log plot of the mobility vs. density for the undoped Si/SiGe heterostructures with the 2DEG at different depths [65]. The color code represents the heterostructures with the 2DEG depth of 10 nm (black open circles), 25 nm (red open circles), 50 nm (brown open circles), and 100 nm (blue open circles). The author used gray, orange, and green dotted lines to highlight the regions where the mobility varies the density following a power-law. Theoretical calculations for the device with the 2DEG depth of ∼50 nm are shown as a solid dark green line. The inset shows the zoom-in data for the 100 nm depth device and the green line indicates the power-law dependence of mobility on the density. Reproduced from [65]. CC BY 3.0.

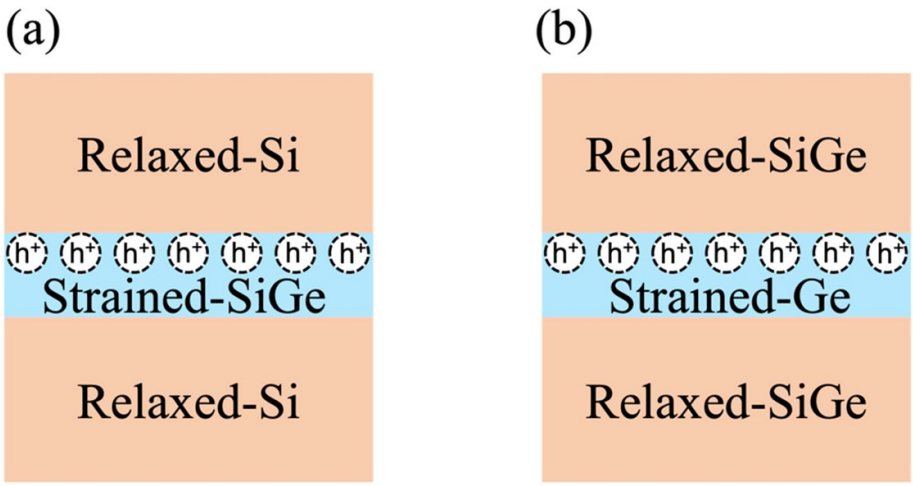

Figure 4. Schematics of (a) relaxed-Si/strained-SiGe/relaxed-Si and (b) relaxed-SiGe/strained-Ge/relaxed-SiGe heterostructures. Holes are confined in the strain-SiGe and Ge layers in (a) and (b), respectively.

limited to below 20 000 cm^2 $(V\,s)^{-1}$ [67] (MOD) due to the strong alloying scattering in the quantum well even though compressive strain leads to a reduced hole effective mass [68]. To eliminate the alloy scattering, the SiGe channel layer for hole transport has been replaced with a pure Ge layer (figure 4(b)) [23] (undoped) [57], (MOD) [58], (undoped). To form a hole quantum well, the Ge layer is compressively strained and two degenerate hole bands (heavy-hole and light-hole) are split [68]. To accomplish this, $Ge_{1-y}Si_y$ relaxed buffer layers must be grown. The Si fraction in this case must be as low as possible (usually 0.2–0.4 [23]) to reduce the lattice mismatch between the GeSi relaxed buffer and strained Ge layers and keep the 2DHG away from material defects such as threading dislocations. However, this requirement sets a limit of epitaxial growth of the GeSi relaxed buffer with a typical grading rate of 10% per micron for the Ge fraction. While this was realized by different growth techniques such as CVD [23, 57, 58] or MBE [69] (MOD), a fairly thick SiGe layer, typically 8–12 μm, is required since a small grading rate of the Ge fraction of GeSi is needed to reduce the threading dislocation defects. Due to the relaxation of strain energy, the GeSi surface will be rough with a root-mean-square (rms) surface roughness of 8–15 nm, a threading dislocation density in the range of 10^6 cm^{-2}, and a typical mobility of ∼120 000 cm^2 $(V{\cdot}s)^{-1}$ [70, 71].

Another way to achieve high-quality GeSi buffer layers is to grow a Ge relaxed buffer via a two-temperature growth method [72], by which dislocations nucleate without enhancing the surface roughness during the initial low-temperature growth stage (∼400 °C). Then another Ge layer was grown at a higher temperature (650 °C–700 °C), followed by a reverse-graded $Ge_{1-y}Si_y$ buffer layer with the Si fraction

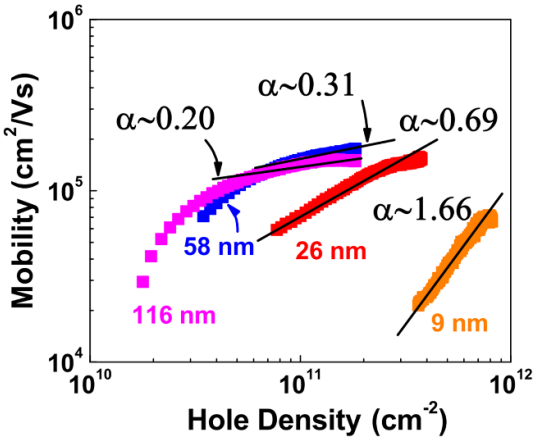

Figure 5. Hole mobility vs. density of the undoped Ge/GeSi heterostructures with different 2DHG depths [23]. The solid black line is derived by fitting the experimental results to $\mu \propto p^{\alpha}$, where μ is the mobility and p is the hole density. Reprinted figure with permission from [23], Copyright (2017) by the American Physical Society.

from zero to the target value. A constant GeSi buffer layer and a thin Ge layer (10–20 nm) are deposited and covered by another GeSi layer as a top cap. In 2012, Dobbie *et al* demonstrated an ultra-high hole mobility exceeding 1000 000 cm^2 $(V\,s)^{-1}$ [57] at 12 K in the strained Ge quantum well. The Ge/GeSi heterostructure was epitaxially growth by CVD and the carriers are supplied via a modulated-doped layer separated from the 2DHG layer with a distance of 30 nm. While the high hole mobility has enabled the opportunity to investigate quantum physics of 2DHG in the Ge channel, the carrier density is relatively high due to the presence of modulation-doped layer compared to the undoped Ge/GeSi heterostructure [23, 58]. Although the precise control over the doping concentration and the distance between the doped layer and Ge layer could modulate the 2DHG density, the lack of the tuning the carrier density in the heterostructure hampers further understanding of the Ge 2DHG. For example, the SOC strength in the Ge layer can be adjusted by varying the gate bias on an undoped Ge/GeSi heterostructure. Furthermore, unlike GaAs/AlGaAs or Si/SiGe heterostructures, the Fermi energy in Ge has high tendency to be pinned at the maximum of the valence band [73], which prohibits effective Schottky gating for Ge-based 2DHG. While a post-growth approach, such as ion implantation [74], to reduce the carrier density below 1.5×10^{11} cm^{-2} was demonstrated with high-quality carrier transport, the induced damage by radiation and the required thermal processes could lead to more material defects and device instability.

In 2016, Laroche *et al* demonstrated an undoped Ge/GeSi heterostructure with a peak mobility of 300 000 cm^2 $(V\,s)^{-1}$ and reduced the carrier density down to 1×10^{10} cm^{-2} [75], an order of magnitude lower than that in a modulated-doped structure. The growth procedure for the undoped structure was similar to the modulation-doped structure and the density dependence of mobility was extracted in figure 5. By varying the distance between the oxide interface and the 2DHG layer, the power-law dependence of mobility on the density shows that for a shallow 2DHG with a depth of 9 nm, the exponent is close to 1.5 while for a deep 2DHG, the exponent increases [23]. This suggests the dominant scattering mechanisms are the remote impurity scattering for a shallow 2DHG and the background impurity scattering for a deep 2DHG, respectively. Clear quantum Hall plateaus and SdH oscillations down to zero were demonstrated, indicating no parallel conduction in the undoped structures.

Using an undoped structure, a lot of quantum physics can be probed by modulating the carrier density via top gating. For example, the SOC strength in the Ge layer was modulated and a ballistic transport of holes was demonstrated [26]. For a lower hole density, only weak localization effect was observed while inducing more holes into the Ge channel strongly enhances the SOC effect. At the same time, the mobility is also boosted due to stronger carrier screening effect, opening up a regime of ballistic spin transport, where the spin-orbit time is shorter than the transport time of carriers (figure 6). By combing the gate-induced SOC physics with spin valves as reservoir, spin FETs on group-IV materials become feasible [76–78].

2.3. GeSn/Ge heterostructures

In 2021, Tai *et al* [30] demonstrates 2DHG in undoped GeSn/Ge heterostructures with clear SdH oscillations and integer quantum Hall effect observed, and the highest mobility of ~20 000 cm^2 $(V{\cdot}s)^{-1}$. Three $Ge_{1-x}Sn_x$/Ge heterostructures with $x = 6\%$, 9%, and 11% were epitaxially grown on Si wafers by CVD (figure 7(a)). The samples were made into an enhancement-mode field effect transistors, and the Hall measurement was conducted to characterize the electro- and magneto- transport properties at 1.2 K.

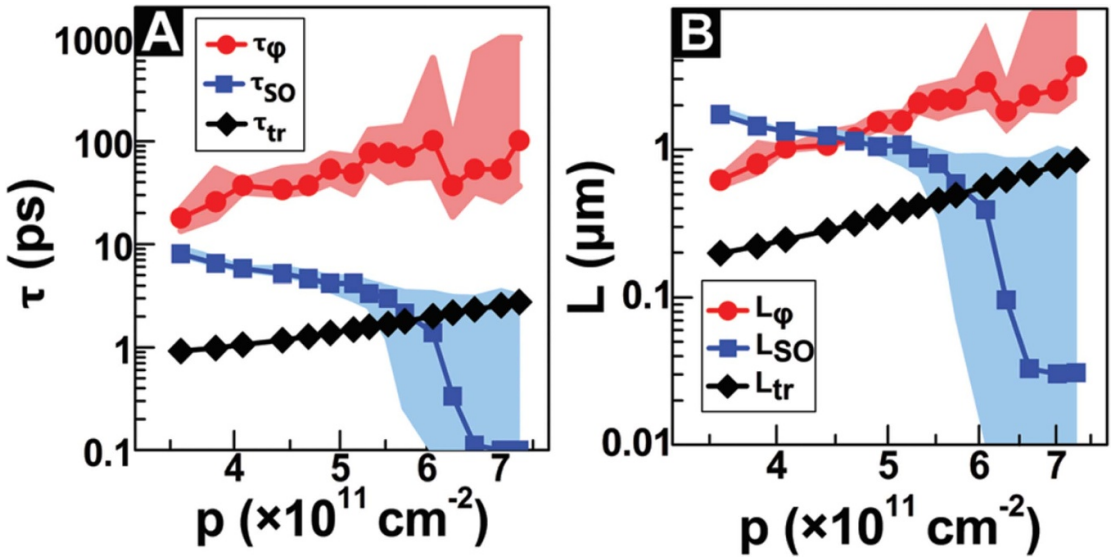

Figure 6. (A) Time and (B) and the corresponding length vs. hole density. The subscripts of φ, SO, and tr represent phase coherence, spin-orbit, and transport properties. Reproduced from [26] with permission from the Royal Society of Chemistry.

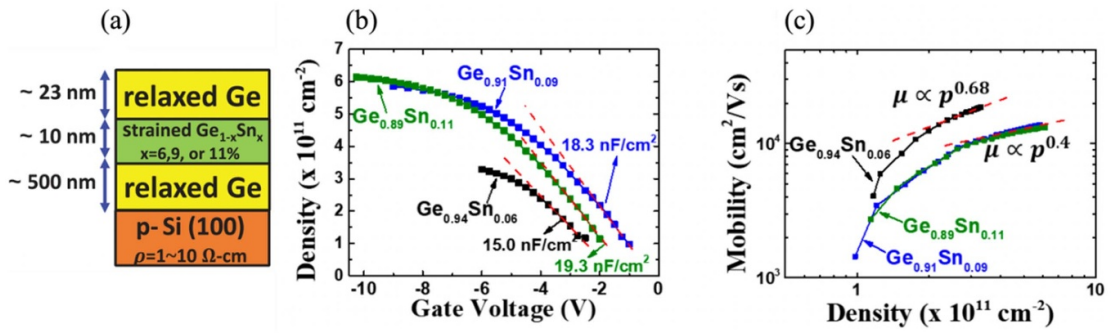

Figure 7. (a) A schematic, (b) Hall density versus gate voltage, and (c) Hall density versus mobility of the GeSn/Ge heterostructure at $T = 1.2$ K. (a)–(c) [30] John Wiley & Sons. © 2021 Wiley-VCH GmbH.

Figure 7(b) shows the Hall density versus gate voltage. As the gate voltage becomes more negative, the hole density increases through capacitive coupling. The effective capacitance is extracted by a linear fit, and the values are 15.0 nF, 18.3 nF, and 19.3 nF cm^2 for the $Ge_{0.94}Sn_{0.06}$, $Ge_{0.91}Sn_{0.09}$, and $Ge_{0.89}Sn_{0.11}$ devices, respectively. This is unexpectedly small compared to the effective series capacitance of Al_2O_3 (in this work, a 90-nm thick Al_2O_3 is deposited as gate oxide) and Ge layers ($C_{\text{eff}} = \frac{1}{\frac{1}{C_{\text{Ge}}} + \frac{1}{C_{Al_2O_3}}} \sim 50$ nF cm^2). This could be attributed to the surface tunneling effect since the top Ge layer is so thin, resulting in a small tunneling barrier. The extracted effective capacitance is larger for the devices with higher Sn fractions, which is due to a smaller tunneling rate by the larger band offset. Moreover, because of the larger band offset at the GeSn/Ge heterojunction, a higher saturation density was achieved for the GeSn device with a higher Sn fraction. A log-log plot of Hall mobility versus density is shown in figure 7(c). The maximum mobilities are above 10 000 cm^2 (V s)$^{-1}$ for all GeSn/Ge heterostructures. As the carrier density increases, the mobility is increased due to the screening effects with the highest mobility of 20 000 cm^2 (V s)$^{-1}$. The mobility is reduced with the Sn fraction in the GeSn QW due to stronger alloy scattering [68, 79]. The dominant scattering mechanism can be characterized by the power-law dependence of mobility on carrier density ($\mu \propto p^{\alpha}$), where p is the hole density. Remote impurity scattering can be characterized with $\alpha \sim 1.5$, while $\alpha \sim 0.5$ refers to background impurity scattering [75]. At a low density, a strong dependence between mobility and density is attributed to the metal-insulator transition (MIT) effect at low temperatures [80]. At a higher density, α gradually saturates to roughly 0.4–0.7, which could be attributed to the background impurity scattering [75]. Figure 8 shows the SdH oscillations and clear integer quantum Hall plateaus for the $Ge_{0.94}Sn_{0.06}$/Ge device.

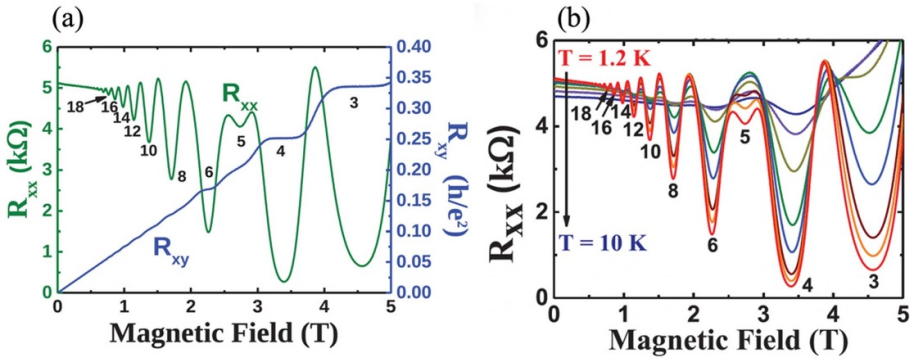

Figure 8. (a) Longitudinal and transverse magneto-resistance and (b) temperature dependence of SdH oscillations of 2DHG in a $Ge_{0.94}Sn_{0.06}$/Ge heterostructure at $T = 1.2$ K. The numbers represent filling factors. [30] John Wiley & Sons. © 2021 Wiley-VCH GmbH.

3. Surface tunnelling in undoped heterostructures

While the purification of ^{28}Si isotopes improves the decoherence time of qubits [10], other factors could also reduce the decoherence time further, such as charge noise [13]. A recent study shows that the coherence time is limited by the charge noise [81] in various operation regimes. Therefore, understanding the source of charge noise becomes crucial for large scale spin-based quantum computing. One of the major sources is the trapped charges (can be electrons or holes) located at the oxide/semiconductor interface. Massai *et al* [82] investigated the impact of the interface charges on the stability of the Coulomb diamond peaks. The authors fabricated a Hall bar device on an undoped Ge/GeSi heterostructure, where the 2DHG is confined in a strained-Ge quantum well. They studied the hole transport properties by performing a measurement cycle including three steps: (1) A negative gate voltage ($V_{\rm min}$) was first applied for 60 s, and then the gate voltage was swept back to zero. (2) The gate voltage was swept from 0 V to $V_{\rm min}$ in steps and R_{xx}, R_{xy}, and I_{xx} are measured. At each voltage, a perpendicular magnetic field was swept from 100 mT to 0 T. (3): A more negative $V_{\rm min}$ is applied to the gate for 60 s, and then sweep the gate voltage back to zero and go to step (2) again (For details of the measurement procedures, readers please refer to [82]). The author defined a turn-on voltage ($V_{t.o.}$) where the I_{xx} reaches 90% of the saturation current. They found $V_{t.o.}$ shifts to a more negative value as they decreased $V_{\rm min}$. They attributed this $V_{t.o.}$ shift to the tunneling of the holes in the Ge QW to the trap states at the oxide/semiconductor interface. This mechanism is known as the surface tunneling effect, which has been discovered only in the undoped systems, such as Si/SiGe [83–86] or Ge/GeSi heterostructures [23]. The trapped charges screen out the gate electric filed, so a more negative $V_{t.o.}$ is needed to turn on the device. The authors further investigated the effects of those interface trapped charges on the QD device. They assessed the charge noise by a similar measurement protocol, where a plunger gate was biased more negatively in each cycle and monitored the Coulomb peaks. They found the amplitude of fluctuations in Coulomb peaks increases for a more negative $V_{\rm min}$, which suggests the interface charges are the source of the noise. They also found that the noise can last for a long period of time (∼40 h), and cannot be eliminated by sweeping back to a zero bias. This study emphasizes the importance of the underlying physics of the surface tunneling of carriers in the buried 2DEG or 2DHG layer and the quality of oxide/semiconductor interface. In this section, we briefly review the physics of the surface tunneling effect in the group-IV undoped heterostructures.

Lu *et al* investigated undoped Si/SiGe heterostructures with various 2DEG depths larger than 100 nm and different Ge fractions [83]. An upper limit of the carrier density with the gate bias was demonstrated (figure 9(a)), which is attributed to the surface tunneling [23, 84, 85]. At cryogenic temperatures, carriers can only be injected to the buried channel from the reservoir. Under a certain gate bias, the carrier density increases with the gate bias while under high gate biases, the density starts to saturate. The simulation based on the Schrodinger-Poisson equations predicted that there exists a maximum density, where the Fermi level is elevated to the ground state of the triangular quantum well at the oxide/Si interface (figure 10). At that point, extra carriers induced by an increased gate bias will flow into the surface channel instead of the buried channel. Then the heterostructure should behave as a bilayer system with two conducting channels: buried

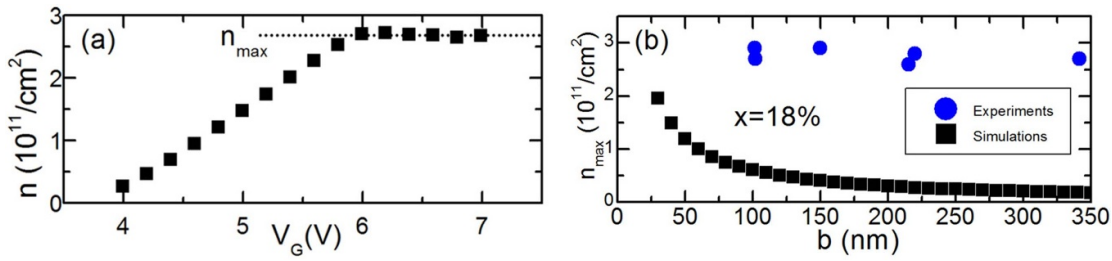

Figure 9. (a) Electron density vs. gate bias and (b) saturated electron density vs. 2DEG depth. Reprinted from [83], with the permission of AIP Publishing.

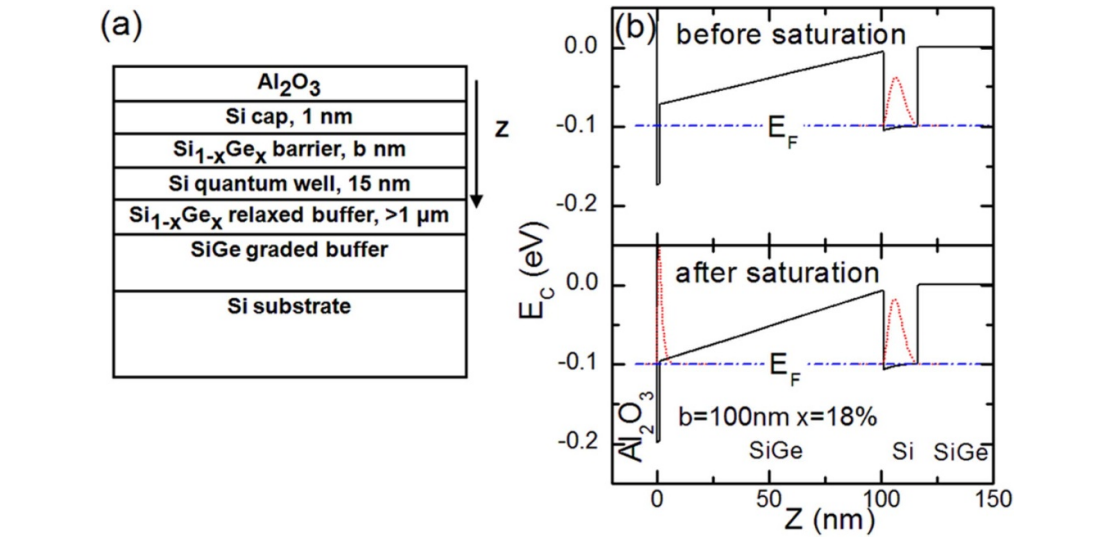

Figure 10. (a) An undoped Si/SiGe heterostructure and (b) the associated simulated band diagrams by Schrodinger-Poisson self-consistent equations. Reprinted from [83], with the permission of AIP Publishing.

2DEG (or 2DHG) and the surface channel. The effective Hall density (n_{eff}) and mobility (μ_{eff}) are given by [87]

$$n_{\text{eff}} = \frac{(n_s\mu_s + n_b\mu_b)^2}{n_s\mu_s^2 + n_b\mu_b^2} \text{ and } \mu_{\text{eff}} = \frac{n_s\mu_s^2 + n_b\mu_b^2}{n_s\mu_s + n_b\mu_b} \tag{1}$$

where n_s (n_b) and m_s (m_b) represent the carrier density and mobility in the surface (buried) channel, respectively. Carriers are injected into the surface channel and an extra gate bias results in a density increase in the surface channel. The carrier density and mobility in the buried channel are then pinned. Since the surface mobility is fairly low compared to that in the buried channel, the effective carrier density is determined by the pinned density and mobility in the buried channel. By increasing the depth of the buried channel, the maximum density should decrease due to the smaller electric field (figure 9(b)).

However, the experimental results of the peak carrier density are higher than the theoretical predictions and independent of the 2DEG depth (figure 9(b)). Due to the proximity to the oxide interface, the surface mobility is much lower than that in the buried mobility and the critical MIT density is much higher. Thus, carriers are unable to flow into the surface layer to form a channel. A non-equilibrium occurs to satisfy the charge conservation with an increasing gate voltage. The carriers tend to flow into the buried channel, enhancing the vertical electric field and leading to the surface tunneling (i.e. carriers in the buried channel tunneling to the surface). Under a low gate bias, the tunneling rate is small, so the carrier loss via surface tunneling is negligible and the carrier density is increased with the gate bias. As the gate bias increases further, more carriers are injected into the buried channel, resulting in a much larger electric field and thus, a much higher tunneling rate. Once a steady-state is established between the carrier injection from the reservoir and the surface tunneling, the carrier density would not be increased. To justify this tunneling process, an insulated-gate field-effect transistor was fabricated and characterized with its DC transport properties at different temperatures [86]. Under a small gate bias, the current increases with the gate voltage

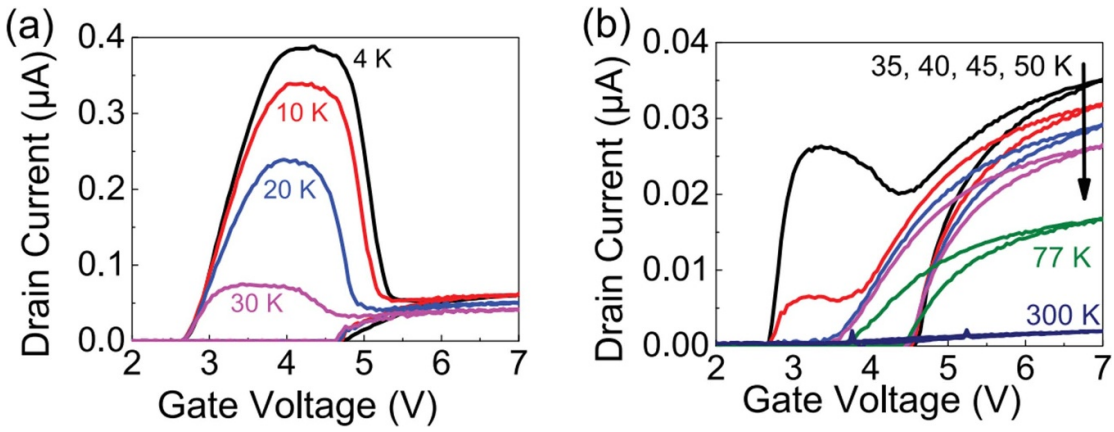

Figure 11. (a) Current vs. gate voltage for an undoped Si/SiGe heterostructure at (a) 4–30 K and (b) 35–300 K. Reprinted from [86], with the permission of AIP Publishing.

followed by a saturation. Then further increasing the gate voltage leads to an abrupt decrease of the current followed by another current saturation (figure 11). At a higher temperature (>50 K), both current plateaus disappear and normal transistor characteristics were observed. The first plateau supports the argument of the surface tunneling of the carriers in the buried channel into the surface channel. With a larger gate bias, the current starts to drop because after the surface tunneling process, those electrons effectively passivate the charged impurities close to the oxide interface, and charge distributions in the two conducting channels can be pushed back to the equilibrium states. Under an even large gate bias, more electrons are introduced to both channels. Since the conductivity in the surface channel is much lower than that in the buried channel, increasing the gate voltage would not lead to a current increase. At a higher temperature, this non-equilibrium is destroyed due to more electrons accumulated in the surface channel, preventing the surface tunneling to occur. Thus, there is no current plateau. A similar carrier transport was observed in undoped Ge/GeSi heterostructures with different depths of 2DHG [23]. Using the parallel capacitor model, the effective capacitance through the slope of the density versus the gate voltage can be extracted to study the carrier distributions. For deep 2DHGs, the extracted capacitance follows the prediction by the parallel capacitor model, but the shallower 2DHGs does not. This strongly suggests the surface tunneling is universal in the undoped heterostructures.

While the DC characteristics of carrier transport did show strong evidence of surface tunneling in the buried 2DEG/2DHG, a more detailed analysis of carrier density by Hall measurements was performed to further verify this interesting physics by Su *et al* [85]. Two undoped Si/SiGe heterostructures with different 2DEG depths of 50 and 100 nm were characterized by Hall measurements under very large gate voltages (up to 10 V) (figure 12). There are four transport regimes: (i) 2DEG screening, (ii) surface passivation, (iii) remote carrier screening, and (iv) parallel conduction and equilibrium (figure 13). In the first regime, electrons are injected into the buried channel and the mobility increases with the carrier density due to the carrier screening effect. At a lower density, the mobility decreases with the density abruptly, showing the MIT characteristics. At the density regime of 1–2 $\times$ 10^{11} cm^{-2} (region I_B in figure 12(c)), the power-law dependence of mobility on the density suggests the remote impurity scattering at the oxide interface is dominant ($\alpha = 1.43$). With a large gate bias, the density becomes saturated while the carrier mobility is increased (region II_A in figure 12). This can be explained by the surface passivation effect. At this point, electrons in the buried channel tunnel to the surface channel and trapped by the midgap defects at the oxide interface. This would smoothen the potential fluctuations by the charged centers at the oxide interface, reducing the impacts on the carriers in the buried channel. Meanwhile, the carrier density stays constant due to the balance between the carrier injection from the reservoir by the top gating and the surface tunneling.

While the passivation of the charged centers at the oxide interface boosts the carrier mobility, increasing the gate bias further would not enhance the mobility, instead, a mobility saturation is observed (region II_B in figure 12). The authors attributed this to the over-compensation by the electrons after tunneling to the surface channel. There are two main types of charged centers at the oxide interface: slow-varying potentials by the oxide charges and deep potential valleys due to the interface charges. As the tunneling occurs at a lower gate bias, electrons tend to be trapped in those deep potential valleys first, leading to a mobility enhancement in the region II_A. Once more electrons tunnel to the surface channel, those deep potential traps would be flattened out, and some of them will be trapped in the slow-varying potential valleys, causing extra potential bumps. Thus, the mobility is not effectively enhanced anymore. At this stage, the exponent of the

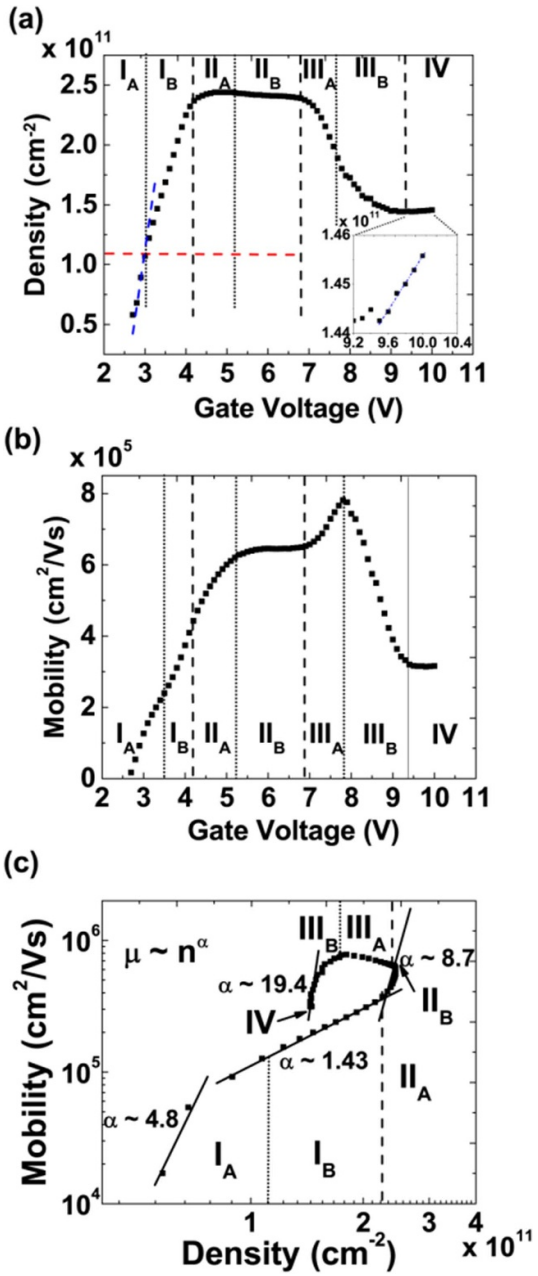

Figure 12. (a) Hall density vs. gate bias, (b) Hall mobility vs. gate bias, (c) and Hall mobility vs. density for an undoped Si/SiGe heterostructure. Reprinted from [85], with the permission of AIP Publishing.

density dependence of mobility is much larger ($\alpha \sim 8.7$), which reflects the fact that the screening charges could not be measured by Hall measurements.

The most striking feature of the surface tunneling physics by Hall measurements is the reduction of carrier density with an increase of carrier mobility as the gate bias increases. This negative density dependence of carrier mobility is usually associated with the alloying scattering or the interface roughness scattering [63]. However, this density regime is too low for both scattering mechanisms to be dominant ($>10^{12}$ cm^{-2}). The carrier density drops due to the carrier loss from the buried channel to the surface channel. In this regime, many electrons tunnel to the oxide interface and passivate the charged centers effectively. Then supplying more electrons to the oxide interface enables the formation of the surface channel. At this stage, localized states are filled and the electrons are injected into the surface channel with a much lower critical density. Since the effective mobility of the surface channel (μ_s) is much lower than that of the buried channel, the effective carrier density (n_{eff}) is determined by the carrier density in the buried channel (equation (1)). Both carrier densities are approximately equal. As the effective carrier density decreases with the gate bias, the carrier screening should become weaker and lead to a reduced mobility. The experimental results show the opposite trend. On the other hand, the carrier loss leads to more electrons

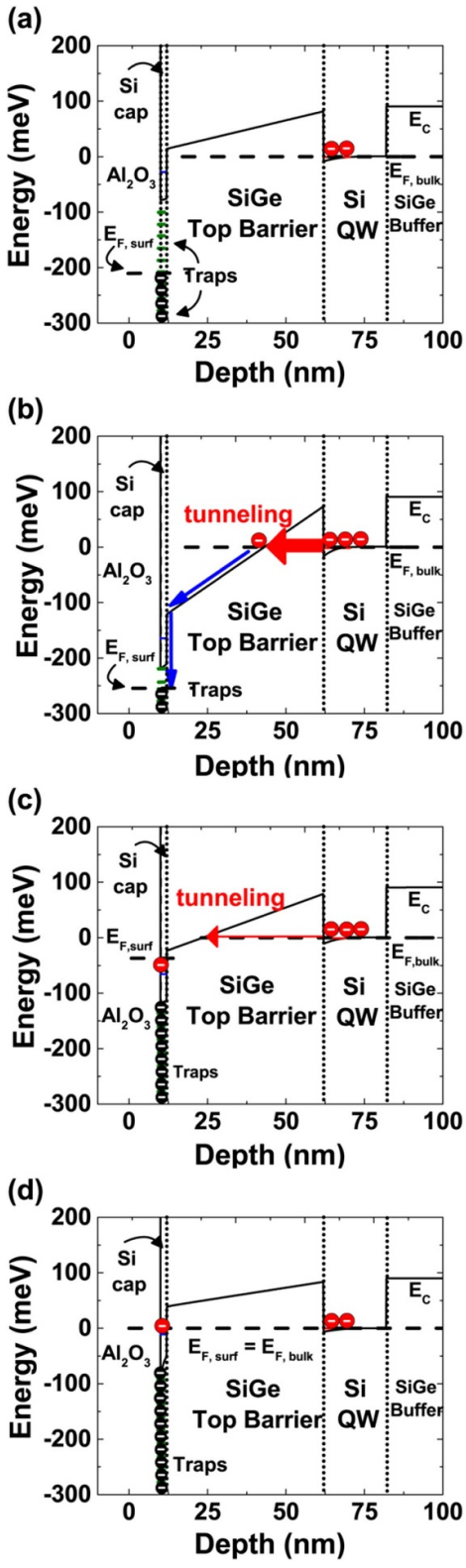

Figure 13. Band diagrams of the undoped Si/SiGe heterostructure at stage (a) I_B, (b) II, (c) III, and (d) IV in figure 12. Reprinted from [85], with the permission of AIP Publishing.

accumulating in the surface channel. While those electrons are mobile, the mobility at the surface channel is still much lower than that in the buried channel. An estimate is made by assuming the channel mobility is 10 000 cm^2 $(V{\cdot}s)^{-1}$ [88], which is a typical number for a Si MOSFET at cryogenic temperatures with a perfectly flat surface with probably the best oxide interface by thermally growing SiO_2. Comparing this mobility with the 2DEG mobility in the buried Si channel (>300 000 cm^2 $(V\ s)^{-1}$), the effective mobility would still be dominated by the buried channel. Thus, the effective mobility should decrease as the carrier

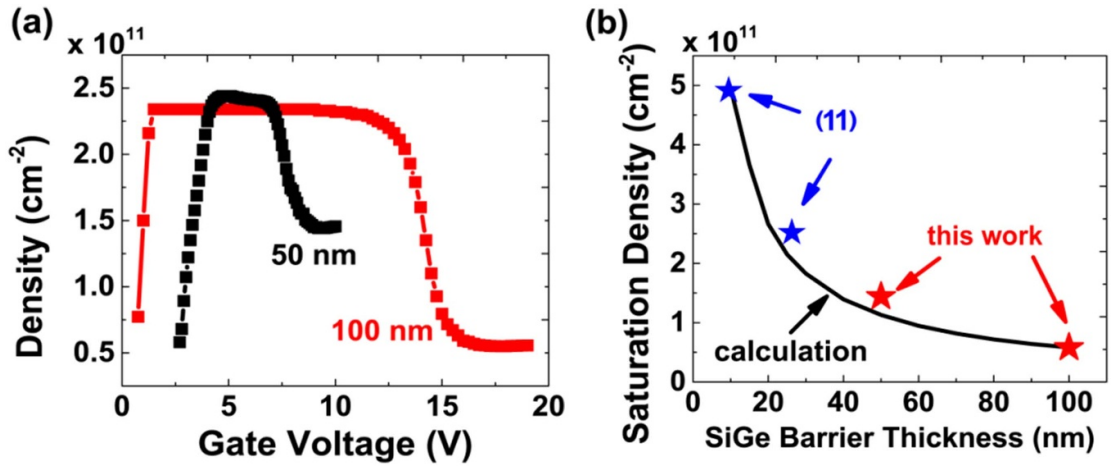

Figure 14. (a) Hall density vs. gate voltage of undoped Si/SiGe heterostructure with two different 2DEG depths, and (b) saturation density at higher gate biases in (a) vs. SiGe barrier thickness (2DEG depth). Reprinted from [85], with the permission of AIP Publishing.

density decreases. They attributed this to the effects of remote screening of the surface carriers on the 2DEG mobility in the buried channel. A proof-of-concept calculation was made to grasp the ideas of this remote screening effects and the negative dependence of the density vs. mobility agrees with the experimental results. Furthermore, the extracted carrier mobility in the surface channel is in the range of 1 000–4 000 cm^2 $(V\ s)^{-1}$, lower than that in the Si MOSFET device. In the undoped Si/SiGe heterostructure without extra polishing steps, the surface is very rough due to the strain relaxation and impurities can be trapped more easily, leading to a lower mobility than that in Si MOSFETs.

During the process of the surface tunneling, the undoped system is bouncing back to the equilibrium. Once the gate voltage is high enough (region IV), the density and mobility become saturated again. At this stage, the Fermi levels in the heterostructure are connected due to the availability of carriers in the surface channel. Any further increment of the gate bias would induce electrons into the surface channel, effectively screening the gate electric field over the buried channel. Since the mobility of the surface channel is much smaller than that in the buried channel, for this bilayer system, the effective mobility is determined by conductance of the buried channel. Due to the effective screening of the surface channel on the buried channel, the density and mobility in the buried channel are pinned. Thus, the effective density and mobility in the undoped heterostructure are constant and equal to the equilibrium values (figure 14).

Hou *et al* utilized this feature in the Si/SiGe undoped heterostructure to demonstrate a novel flash memory device at cryogenic temperatures (below 40 K) [89]. For a gate-effect transistor, the charge distributions in the regions between the metal gate and the conduction channel determine the threshold voltage [90]. By biasing the device under a reasonably high gate voltage, carriers in the buried channel tunnel to the oxide interface and are trapped there, increasing the threshold voltage (figure 15). Programming and erasing steps are performed to induce and deplete electrons at the Si surface channel and high endurance of $>10^4$ cycles and long retention times of 10^4 s were demonstrated. C–V characteristics show the transition of the charge distribution in the buried and surface channels [90] and support the previous arguments by Hall measurements [85]. For conventional non-volatile flash memory devices, an oxide layer is used as a tunneling barrier, which suffers severe reliability issues since during the tunneling processes, electrons could be trapped and modify the charge distributions in the oxide layer. For the undoped Si/SiGe heterostructure, due to the much higher crystal quality and few defect states in the crystalline SiGe layer, excellent device stability is expected.

4. Hole effective mass in Ge 2DHG

Effective mass is one of the most fundamental physical parameters for material science and quantum technologies. The value of effective mass is proportional to the reciprocal of a second-order derivative of energy (E) with respect to momentum (k), given by $m^* = [\frac{1}{\hbar^2}\frac{d^2E}{dk^2}]^{-1}$ [91]. For group-IV atoms (Si and Ge), two valence electrons occupy an *s*-orbital while the other two occupy *p*-orbitals. The s-orbital and three *p*-orbitals (p_x, p_y and p_z) are hybridized to form sp^3 orbitals. For group-IV crystals, this hybridization leads to an 'anti-bonding' conduction band and a 'bonding' valence band [87]. A key feature is that the conduction band has *s*-orbital like symmetry and the valence band has *p*-orbital like symmetry. We focus on the valence

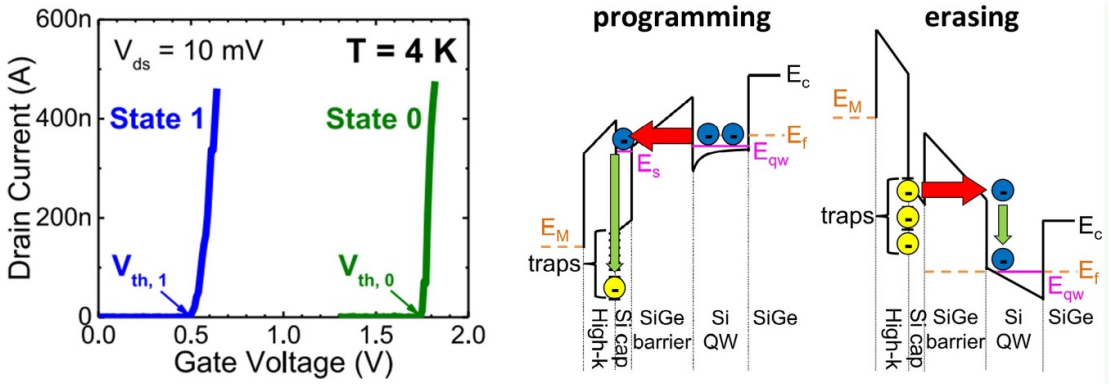

Figure 15. (a) *I–V* characteristics for two states (state 1 and 0) in a Si/SiGe flash memory device and (b) band diagrams to show programming and erasing steps. Reprinted with permission from [89]. Copyright (2022) American Chemical Society.

band structure of Ge owing to its versatile applications on high-mobility transistors [92], SOC [93], and qubit devices [15, 16, 29].

The simplest model for the valence band structure is the Kane model [87]. However, the Kane model ignores the SOC effects [87]. The Lüttinger–Kohn Hamiltonian [94], an extension of the Kane model, takes the SOC effects into account. As described before, the valence band is p-orbital like and has an orbital quantum number $l = 1$ and $m_l = 1, 0, -1$, and spin quantum numbers of $s = 1/2$ and $m_s = \pm 1/2$. We can assume the QW structure is grown along the z, namely [001] direction. The bases of Lüttinger–Kohn Hamiltonian are chosen as the total angular momentum (j) and the projection along the z-direction (m_j). The total angular momentum is $j = l + s$, which can be 3/2 or 1/2. For $j = 3/2$ state, possible m_j are $\pm\frac{3}{2}$ and $\pm 1/2$. For $j = 1/2$ state, m_j is $\pm 1/2$. The six bases are $\left\{ \left|\frac{3}{2}, \frac{3}{2}\right\rangle, \left|\frac{3}{2}, \frac{1}{2}\right\rangle, \left|\frac{3}{2}, \frac{-1}{2}\right\rangle, \left|\frac{3}{2}, \frac{-3}{2}\right\rangle, \left|\frac{1}{2}, \frac{1}{2}\right\rangle, \left|\frac{1}{2}, \frac{-1}{2}\right\rangle \right\}$. The $\left|\frac{3}{2}, \frac{\pm 3}{2}\right\rangle$ $\left|\frac{3}{2}, \frac{\pm 1}{2}\right\rangle$, and $\left|\frac{1}{2}, \frac{\pm 1}{2}\right\rangle$ states represent heavy-hole (HH), light-hole (LH), and split-off bands, respectively [43, 44]. The valence-band Hamiltonian can be expanded to form the 6×6 Lüttinger–Kohn Hamiltonian using these bases [37]:

$$
\begin{array}{c}
 \\
\left\langle \frac{3}{2}, \frac{3}{2}\right| \\
\left\langle \frac{3}{2}, \frac{1}{2}\right| \\
\left\langle \frac{3}{2}, \frac{-1}{2}\right| \\
\left\langle \frac{3}{2}, \frac{-3}{2}\right| \\
\left\langle \frac{1}{2}, \frac{1}{2}\right| \\
\left\langle \frac{1}{2}, \frac{-1}{2}\right|
\end{array}
\begin{array}{c}
\begin{array}{cccccc}
\left|\frac{3}{2}, \frac{3}{2}\right\rangle & \left|\frac{3}{2}, \frac{1}{2}\right\rangle & \left|\frac{3}{2}, \frac{-1}{2}\right\rangle & \left|\frac{3}{2}, \frac{-3}{2}\right\rangle & \left|\frac{1}{2}, \frac{1}{2}\right\rangle & \left|\frac{1}{2}, \frac{-1}{2}\right\rangle
\end{array} \\
\begin{bmatrix}
P+Q & -S & R & 0 & -S/\sqrt{2} & \sqrt{2}R \\
-S^* & P-Q & 0 & R & -\sqrt{2}Q & -\sqrt{2}Q \\
R^* & 0 & P-Q & S & \sqrt{3/2}S^* & \sqrt{2}Q \\
0 & R^* & S^* & P+Q & -\sqrt{2}R^* & -S^*/\sqrt{2} \\
-S^*/\sqrt{2} & -\sqrt{2}Q^* & \sqrt{3/2}S & -\sqrt{2}R & P+\Delta_0 & 0 \\
\sqrt{2}R^* & \sqrt{3/2}S^* & Q^* & -S/\sqrt{2} & 0 & P+\Delta_0
\end{bmatrix}
\end{array}
\tag{2}
$$

where

$$
\begin{aligned}
P &= \tfrac{\hbar^2}{2m_0}\gamma_1\left(k_x^2+k_y^2+k_z^2\right), \qquad Q = \tfrac{-\hbar^2}{2m_0}\gamma_2\left(2k_z^2-k_x^2-k_y^2\right) \\
R &= \sqrt{3}\tfrac{\hbar^2}{2m_0}\left[-\gamma_2\left(k_x^2-k_y^2\right)+2i\gamma_3 k_x k_y\right], \; S = \sqrt{3}\tfrac{\hbar^2}{2m_0}\gamma_3\left(k_x-ik_y\right)k_z
\end{aligned}
\tag{3}
$$

γ_1, γ_2, and γ_3 are Lüttinger parameters ($\gamma_1 = 13.38$, $\gamma_2 = 4.24$, and $\gamma_3 = 5.69$ for Ge [95]). Δ_0 is the energy difference between the split-off band and HH (LH) bands at the Γ point. Δ_0 of Ge is ∼300 meV at room temperature [37]. This shows the split-off band is far away from the HH and LH bands in energy, so the coupling between them can be ignored and only the top left 4×4 matrix is considered [96]. The P + Q (or P−Q) term describes the kinetic energy of the HH (or LH) bands. The S term describes the HH-LH coupling with the same spin orientations, and the R term describes the HH-LH coupling with the opposite spin orientations. The off-diagonal terms lead to the anisotropic band in the $k_x - k_y$ plane. k_x, k_y and k_z are no longer symmetric, and this results in different effective masses along the out-of-plan and in-plane directions. The out-of-plane hole effective mass is given by $m^*_{HH(LH),z} = m_0/(\gamma_1 \mp 2\gamma_2)$, while the in-plane mass is given by $m^*_{HH(LH),xy} = m_0/(\gamma_1 \pm \gamma_2)$ [43, 96]. The smaller in-plane effective mass in the HH band has been demonstrated experimentally [34]. In addition, space confinement and strain are two common constraints in a QW structure, breaking the degeneracy and inducing an energy splitting (∼100 meV [37])

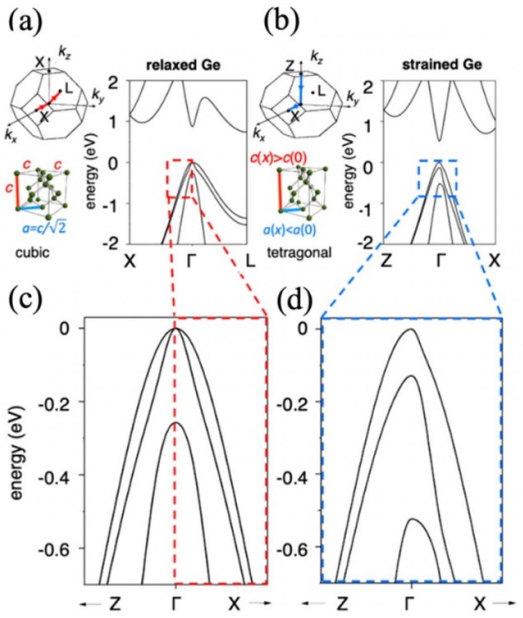

Figure 16. Simulated valence band structures by the density functional theory for (a) relaxed and (b) uniaxially strained Ge and their zoom-in in (c) and (d), respectively. Reprinted figure with permission from [37], Copyright (2021) by the American Physical Society.

between the HH band and LH band. The HH states are energetically favored since it has a larger out-of-plane mass. Strain effect can be described by the Pikus–Bir Hamiltonian [97, 98] with additional terms (P_ϵ, Q_ϵ, R_ϵ and S_ϵ) added into the Lüttinger Hamiltonian (e.g. $P \to P + P_\epsilon$):

$$\begin{aligned} P_\epsilon &= -a_v\left(\epsilon_{xx}+\epsilon_{yy}+\epsilon_{zz}\right),\ Q_\epsilon = \frac{-b_v}{2}\left(\epsilon_{xx}+\epsilon_{yy}-2\epsilon_{zz}\right) \\ R_\epsilon &= \frac{\sqrt{3}}{2}b_v\left(\epsilon_{xx}-\epsilon_{yy}\right) - id\epsilon_{xy},\ S_\epsilon = -d_v\left(\epsilon_{xz}-i\epsilon_{yz}\right) \end{aligned} \tag{4}$$

where $a_v = 2.0$ eV, $b_v = -2.16$ eV, and $d_v = -6.06$ eV [68] are the deformation potentials for Ge. The Pikus-Bir term induces additional offsets and coupling for the HH and LH states. A commonly used assumption is that Ge QW is under biaxial stresses ($\epsilon_{xx} = \epsilon_{yy}$, $\epsilon_{zz} = (-2C_{12}/C_{11})\,\epsilon_{xx}$ and $\epsilon_{ij} = 0$ if $i \neq j$). This makes the non-diagonal terms in the Pikus–Bir Hamiltonian become zero and simplifies the calculation. For Ge, $C_{11} = 129.2$ GPa and $C_{12} = 47.9$ GPa are the elastic stiffness constants [99]. The strain effect leads to anisotropicity in the valence band [11]. In [37], Terrazos *et al* considered a Ge layer grown on a relaxed Si_xGe_{1-x} layer and assumed uniaxial and compressive strains along the growth direction [001] ($\epsilon_{zz} = (-2C_{12}/C11)\,\epsilon_{xx}$) to simulate the band structures through a density functional theory (DFT) method. The ϵ_{xx} is defined as $\epsilon_{xx}\left(=\epsilon_{yy}\right) = \epsilon(x) = \left[a(x) - a(0)\right]/a(0)$ for Si_xGe_{1-x} alloys. The lattice constant $a(x)$ is estimated by the Vegard's law. Figure 16 shows that the Ge valence band becomes anisotropic under stresses and figure 17 shows that the effective mass is reduced as the strain increases.

Experimentally, one can analyze the temperature dependence of Shubnikov-de Haas oscillations to extract the effective masses [100]. The longitudinal magneto-resistance follows the expression: $\Delta R_{xx}/R_0 \propto \chi/\sinh(\chi)$ where $\chi = 2\pi^2 k_B T/\hbar\omega_c$ and $\omega_c = eB/m^*$ is the cyclotron frequency. R_0 represents the monotonic trend of the oscillating R_{xx}, and ΔR_{xx} is the deviation at the maximum or minimum [101]. Sawano *et al* extracted experimentally the hole effective masses in the $Ge/Si_{1-x}Ge_x$ QW structures [36]. Figure 18(a) illustrates the hole effective mass versus hole density under different strain conditions with numbers specifying the Ge fractions of the $Si_{1-x}Ge_x$ buffers. The blue lines are the calculation results with a given Ge concentration. Figure 18(b) shows the strain dependence of the effective mass with a hole density of 2×10^{12} $cm^{-2.}$ The red dots are extrapolated from the experimental results of effective mass from figure 18(a), which qualitatively matches with the calculation results (the blue line). Both figures show that the hole effective mass decreases with strain by reducing the Ge fraction in the SiGe buffer.

The hole effective mass slightly changes with the hole density (figure 18(a)). This results from band non-parabolicity, which originates from the band mixing [102] and results in a linear increase of the effective mass with the carrier density [34, 103, 104]. In [103], Rößner *et al* extracted the hole effective mass which increases from 0.1 m_0 to 0.17 m_0 with the hole density ranging from 2.9×10^{11} cm^{-2}–1.9×10^{12} cm^{-2}

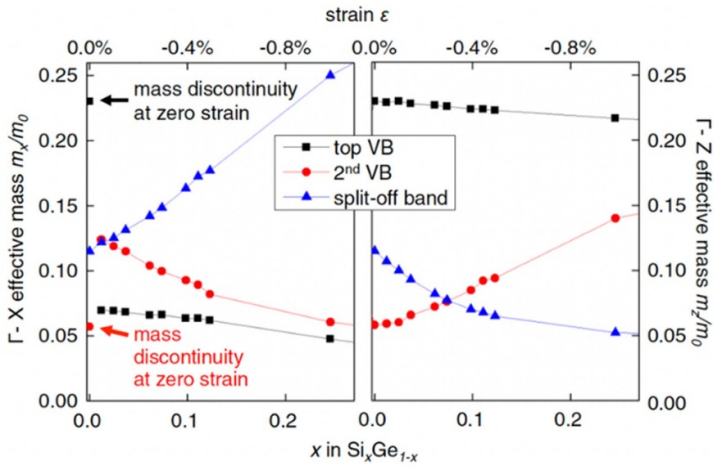

Figure 17. Hole effective masses vs. Si fraction in Si_xGe_{1-x} by DFT. The discontinuity near zero strain shows the inversion of the effective mass due to the band hybridization. Reprinted figure with permission from [37], Copyright (2021) by the American Physical Society.

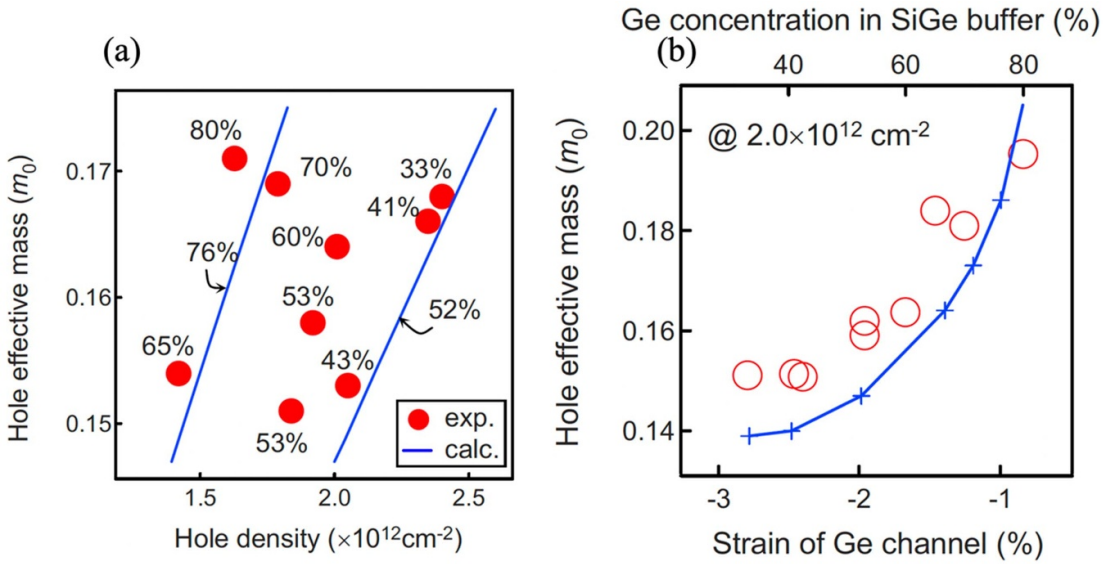

Figure 18. (a) Hole effective mass vs. hole density with different Ge fractions in the $Si_{1-x}Ge_x$ buffer layer and (b) hole effective mass vs. strain with a hole density of 2×10^{12} cm^{-2}. Reprinted from [36], with the permission of AIP Publishing.

(figure 19(a)). The device is modulation doped with a strained Ge QW layer grown on a relaxed $Si_{0.3}Ge_{0.7}$ buffer. They used the linear fit and extrapolation at the Γ point to get a hole effective mass of 0.08 m_0, close to the theoretical prediction (0.098 m_0 [105]) and attributed the difference to the band mixing. They treated $k_{\|} \neq 0$ as perturbations to estimate the band nonparabolicity factor (b), which is defined as $\frac{\hbar^2 k_{\|}^2}{2m_0^*} \equiv E(E+bE)$ [105]. The extracted $b = 9.3$ eV^{-1} is smaller than the predicted value of 12 eV^{-1}, and they attributed this deviation to the quantum well shape, which is triangular not rectangular considered in the analytical model. A more recent work [34] showed the non-parabolicity effect in an undoped $Ge/Si_{0.2}Ge_{0.8}$ QW. In figure 19(b), the density varies from 2.0×10^{11} cm^{-2}–1.1×10^{12} cm^{-2} and the hole effective mass increases from ∼0.06 m_0 to 0.12 m_0. Compared to the prior work [41], where m^* was extracted to be 0.09 m_0 at a density of 5.4×10^{11} cm^{-2}, the effective mass is further reduced at a lower carrier density. They performed a linear fit and extracted a very small mass of 0.048 m_0 at the Γ point. They also demonstrated weak magnetic-field dependence of the effective mass under the magnetic field ⩽4 T (figure 19(c)).

Overall, the hole effective mass depends on many factors since the valence band structure is more complicated than the conduction band. A thorough calculation which considers the quantum confinement, strained effect, valence-band anisotropy, and non-parabolicity can be found in [105].

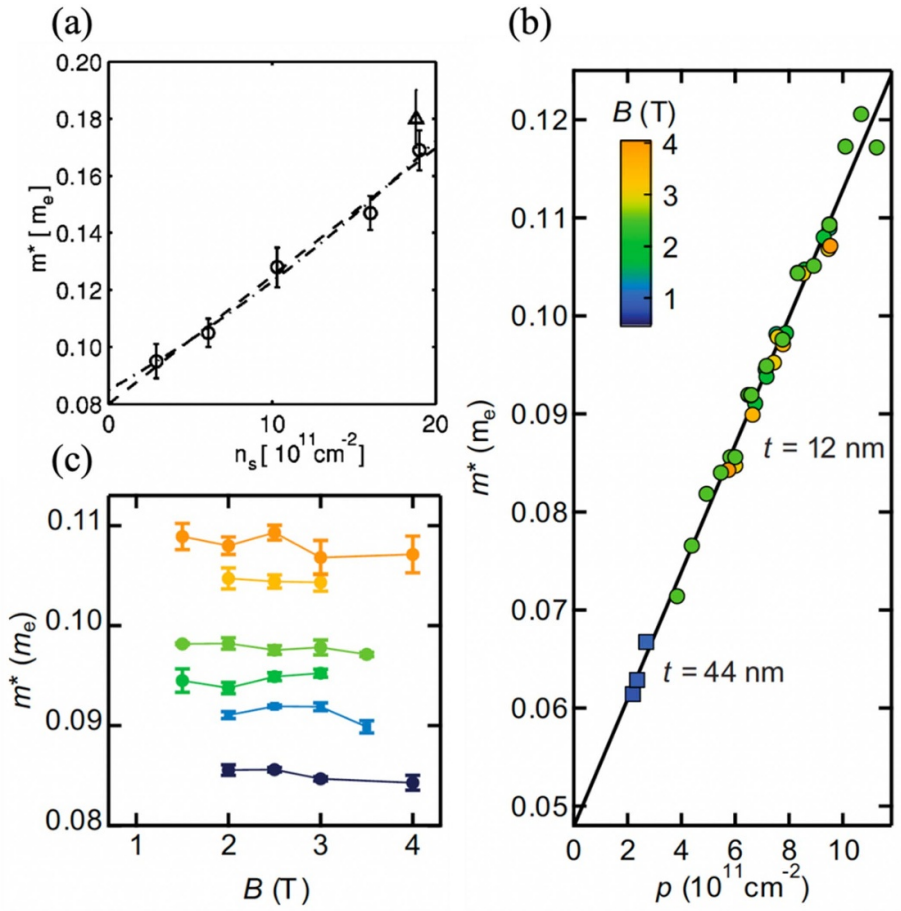

Figure 19. Hole effective mass vs. hole density from (a) [103] and (b) [34]. (c) Hole effective mass vs. magnetic field. Different color represents different hole densities from 5.8 × 10^{11} cm^{-2} (dark blue) to 9.5 × 10^{11} cm^{-2} (orange). Reprinted from [102], with the permission of AIP Publishing. Reprinted figure with permission from [34], Copyright (2019) by the American Physical Society.

5. SOC in Ge-based heterostructures

Spin degeneracy in the band structure is the consequence of both time reversal symmetry and space inversion symmetry [106]. Time-reversal operation changes the sign of $\vec{k}$ and flips the spin orientation, so we have $E(+\vec{k},\uparrow) = E(-\vec{k},\downarrow)$ if the time reversal symmetry holds. Space-inversion operation only changes the sign of $\vec{k}$ with the spin orientations reserved, so $E(+\vec{k},\uparrow) = E(-\vec{k},\uparrow)$. The combination of these two symmetries gives $E(+\vec{k},\uparrow) = E(+\vec{k},\downarrow)$, leading to a two-fold spin degeneracy. A common approach to breaking the spin degeneracy is to apply an external magnetic field to break the time reversal symmetry. The spin degeneracy can be lifted even under a zero magnetic field by removing the space inversion symmetry. The asymmetry usually comes along with an electric field in the system. For carriers (holes, in the Ge-based heterostructures) moving in the channel, they feel an effective magnetic field under the Lorentz transformation [106]. Thus, the hole spin couples to the in-plane motion and this results in the SOC effect. There are two major types of SOC: Dresselhaus SOC [107] and Rashba SOC [108]. Dresselhaus SOC arises from the bulk inversion asymmetry (BIA) [107], which exists in semiconductors with zinc blende structures (e.g. GaAs, InAs) due to the lack of inversion symmetry points in the crystal. For this type of crystal structures, there is an effective built-in electric field and one cannot eliminate or tune the strength of Dresselhaus SOC. On the other hand, the Rashba SOC originates from the structural inversion asymmetry (SIA) [42], which can be manipulated through electric gating. For group-IV materials, there is no Dresselhaus SOC term because the diamond structure has an inversion symmetry point and BIA does not exists [106]. This enables the tunability of SOC strength. We focus on the analysis of Rashba SOC in the Ge-based heterostructures in this review.

There are three bands for the valence band structure: HH band, LH band, and split-off band [87]. The Rashba SOC Hamiltonian has different expressions for HH and LH bands [24, 106]. For the HH band, the Hamiltonian is $H_{HH} = i\alpha_3 E_z \left(k_-^3\sigma_+ - k_+^3\sigma_-\right)$, where α_3 is the k-cubic Rashba coefficient, E_z is the electric field, $k_\pm = k_x \pm ik_y$, and $\sigma_\pm = 1/2(\sigma_x \pm i\sigma_y)$. This results in a k-cubic dependence of the spin-splitting

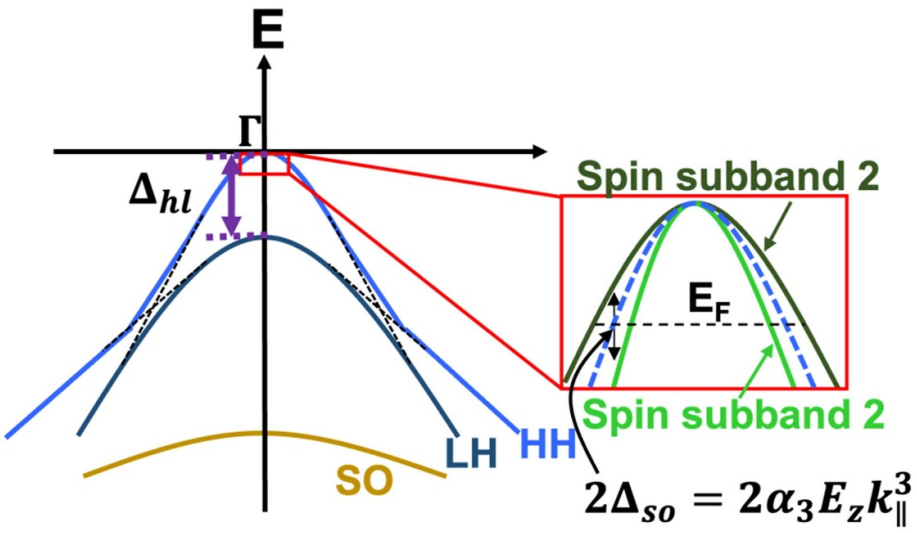

Figure 20. A schematic of valence band structure of compressively strained Ge. The inset shows the zoom-in of HH-band structure without (blue) and with (green) SOC effects near the Γ point. [30] John Wiley & Sons. © 2021 Wiley-VCH GmbH.

energy in the HH band given by $E_{HH} = \pm\alpha_3 E_z k_{\parallel}^3$ [106]. For the LH band, the Rashba Hamiltonian is $H_{LH} = i\alpha_1 E_z (k_- \sigma_+ - k_+ \sigma_-)$, where α_1 is the k-linear Rashba coefficient. The spin-splitting energy in the LH band is given by $E_{LH} = \pm\alpha_1 E_z k_{\parallel}$ [106]. The band structure of Ge is depicted in figure 20. The HH and LH degeneracy at the Γ point breaks in the QW structure [87] and the two bands are separated by Δ_{hl}. The inset of figure 20 shows the spin splitting of the HH band. The blue-dashed line represents the HH band without Rashba SOC while the other two solid lines are two spin subbands when considering SOC effect. The figure shows that the SOC effect lifts the degeneracy of spins and the energy splitting at a given $k_{\parallel}$ is given by $2\alpha_3 E_z k_{\parallel}^3 \equiv 2\Delta_{so}$ [109]. To characterize the SOC effect, one can extract the k-cubic Rashba coefficient (α_3) through weak localization (WL)/weak anti-localization (WAL) patterns [24, 26, 109–112], the beatings of Shubnikov-de Haas oscillations [25, 113], or the cyclotron resonance [114]. In this review, we focus on the first two techniques.

In [24], Moriya *et al* used the WL and WAL effects to extract α_3 in an undoped Ge/$Si_{0.5}Ge_{0.5}$ QW structure. Figure 21(a) shows the magneto-conductivity at different gate voltages. The topmost trace shows the WL effect where the magneto-conductivity increases with the magnetic field. As the gate voltage is reduced, the WL effect becomes weaker and the WAL is more pronounced. The WAL pattern manifests as the magneto-conductivity decreases with the magnetic field first and then increases later. The physical pictures of WL and WAL are explained as follows. For the hole transport in a two-dimensional disordered system, the time-reversal symmetric paths need to be considered [115]. If the perimeter of the loop (L) is smaller than the phase coherence length (L_ϕ), wavefunctions travelling clockwisely and counter-clockwisely are in phase. Constructive interference occurs and the hole wavefunction is 'localized' in space. The interference is a quantum mechanical effect, so the value of conductivity cannot be considered classically [115]. The hole wavefunction is confined in space due to the WL effect, so it cannot propagate through the channel to contribute to the conductivity. By taking the interference effect into accounts [115], the conductivity becomes smaller than the classical value. When a magnetic field is applied, the extra Aharonov–Bohm (AB) phase randomizes the phase and the constructive interference is destroyed, so the magneto-conductivity gradually increases back to the classical value, which is known as the WL effect.

We now consider the SOC effect and the WAL patterns. Holes feel an effective magnetic field due to the SOC effect and their spins couple to the effective field. The direction of the effective field depends on its motion (from Lorentz transformation of the electric field) [116], so the hole spin couples to a randomly changing magnetic field (associated with a transport lifetime, τ_{tr}) and finally the spin state relaxes. This relaxation process is characterized by the spin-relaxation time (τ_{so}). We can define a spin-relaxation length [24] ($L_{so} = \sqrt{D\tau_{so}}$, where $D = {v_F}^2 \tau_{tr}/2$ is the diffusion coefficient and v_F is the Fermi velocity) and compare it to L and L_ϕ. If a hole travels in a loop with a perimeter $L_{so} < L < L_\phi$, the spin state is already relaxed with the single loop, but the two counter-propagating wavefunctions are still in-phase. The relaxation of spins adds an additional phase difference of π, so the interference becomes destructive. The detail of mathematical treatments can be found in [115]. By including this destructive interference, holes are not 'localized', so the magneto-conductivity is larger than the classical value. Similarly, the AB phase randomizes the interference

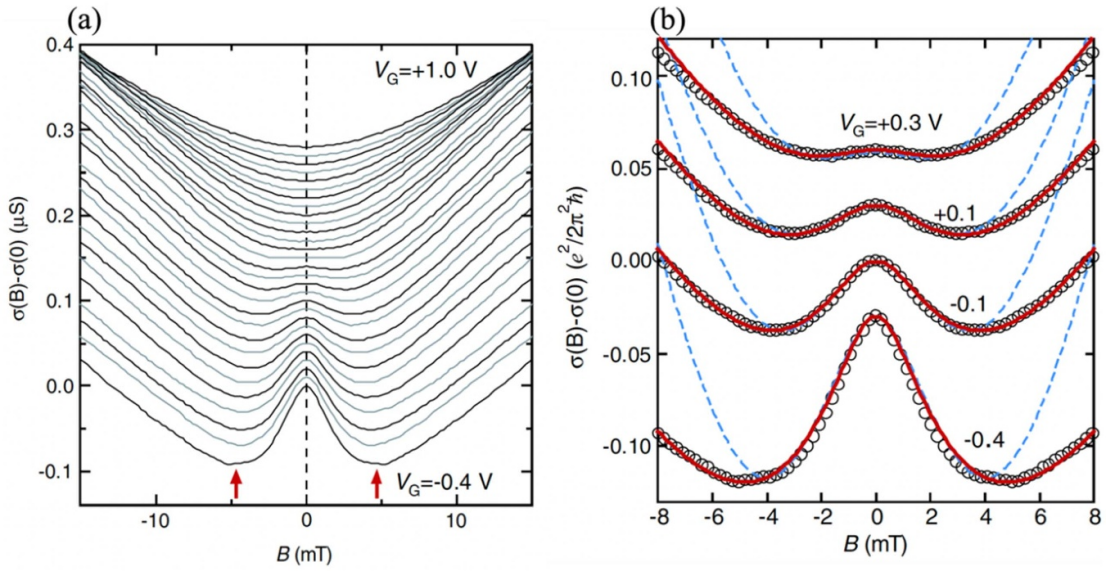

Figure 21. (a) The evolution of magneto-conductance with gate voltage (V_G). A transition from WL to WAL is observed as V_G decreases. (b) The fitting results using the ILP model. The open circles are the experiment data. The red solid lines were obtained using B_ϕ and B_{so3} and the blue dash lines are using B_ϕ and B_{so1}. Reprinted figure with permission from [24], Copyright (2014) by the American Physical Society.

patterns, so the conductivity decreases with the magnetic field. Figure 21(a) shows that the WAL pattern becomes more pronounced as V_G becomes more negative. Since the stronger the SOC effect is, the shorter the L_{so} is. Thus, more loops satisfy the condition of $L_{so} < L < L_\phi$ and the WAL effect becomes stronger. Moreover, the AB phase is proportional to the enclosed area by the loops, so for a larger loop (longer L), its interference patterns become unobservable. The turning points of the WAL patterns in figure 21(a) indicate that the magnetic field is high enough to destroy the interference for the case with the smallest loop which satisfies $L_{so} < L < L_\phi$. If the magnetic field is further enhanced, the AB phase washes out the interference of the loops having $L < L_{so} < L_\phi$. Since the spin state is not relaxed for those loops, the WL effect is observed with an increase of magneto-conductivity.

To quantify the SOC effect, the Iordanskii–Lyanda-Geller–Pikus (ILP) theory was used to fit the WL/WAL patterns [109, 117–119]. In the ILP theory, both the k-linear and k-cubic Rashba terms are included. The complete form of the ILP formula can be found in [24]. There are three parameters B_ϕ, B_{so1}, and B_{so3} in the ILP formula. $B_\phi = \hbar/4eD\tau_\phi$ characterizes the phase coherence time. τ_ϕ links to the coherence length by $L_\phi = \sqrt{D\tau_\phi}$ [26]. $B_{so1(3)} = \hbar/4eD\tau_{so1(3)}$ is the k-linear (cubic) term of Rashba SOC with $\tau_{so1(3)}$ as the spin-relaxation times. The red fitting curves in figure 21(b) are obtained using B_ϕ and B_{so3} terms while the blue dashed lines are obtained by B_ϕ and B_{so1} terms. The better fit using the k-cubit terms (red curve) suggests that the SOC effect is dominated by the k-cubic Rashba SOC.

There are two major types of spin-relaxation mechanisms. First, the D'yakonov–Perel (DP) mechanism [120] assumes that the spin relaxation occurs between collisions and predicts that τ_{so3} is inversely proportional to τ_{tr} ($1/\tau_{so3} = 2|\Omega_3|^2\tau_{tr}$ [26]). Second, the Elliot–Yafet mechanism [121, 122], assumes that the spin-relaxation occurs due to the impurity scattering and predicts $\tau_{so3} \propto \tau_{tr}$. Figure 22(a) shows that $\tau_{so3} \propto 1/\tau_{tr}$, so the spin-relaxation mechanism can be described by the DP mechanism. The spin-splitting is then calculated by $\pm\Delta_{so} = \pm\hbar\Omega_3 = \pm\alpha_3 E_z {k_F}^3$, and with a $\Delta_{so} = 0.39$ meV extracted at a carrier density of 1.5×10^{12} cm^{-2}. The density dependence of Δ_{so} is shown in figure 22(b), where the Δ_{so} increases with the carrier density. Figure 22(c) shows how $\alpha_3 E_z$ changes as a function of carrier density. A decrease of $\alpha_3 E_z$ is observed, which is attributed to the decrease of the electric field instead of α_3. Finally, α_3 for the first HH band is derived as follows:

$$\alpha_3 = \frac{-3e\hbar^4\gamma_3^2}{2m_0(E_{HH} - E_{LH})^2} \tag{5}$$

where γ_3 is the Lüttinger parameter and $E_{HH} - E_{LH} = \Delta_{hl}$ is the splitting between the HH and LH bands. Equation (5) predicts that the cubic-Rashba coefficient should be suppressed by a large Δ_{hl}, which has been observed in a 2DHG in the GeSn/Ge heterostructure in [30]. This is the result of two competing quantization axes. One is along the growth direction (z-axis) by Δ_{hl} and the other is along the in-plane direction by the

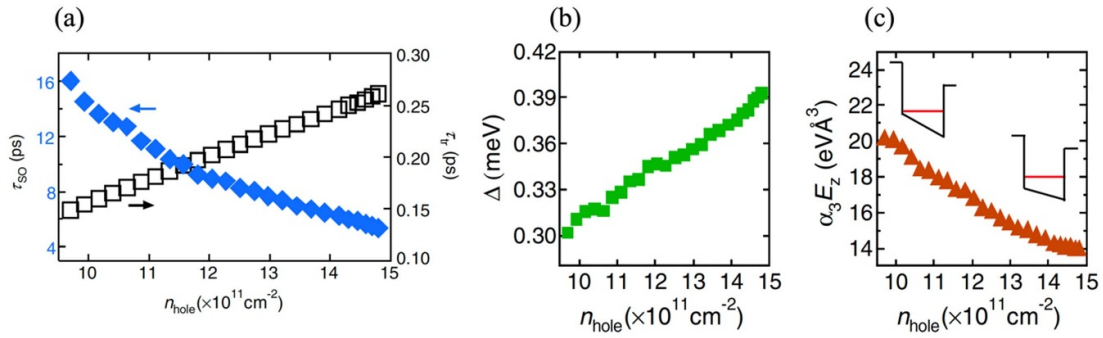

Figure 22. Density dependence of (a) τ_{so} and τ_{tr}, (b) Δ_{so}, and (c) $\alpha_3 E_z$. Reprinted figure with permission from [24], Copyright (2014) by the American Physical Society.

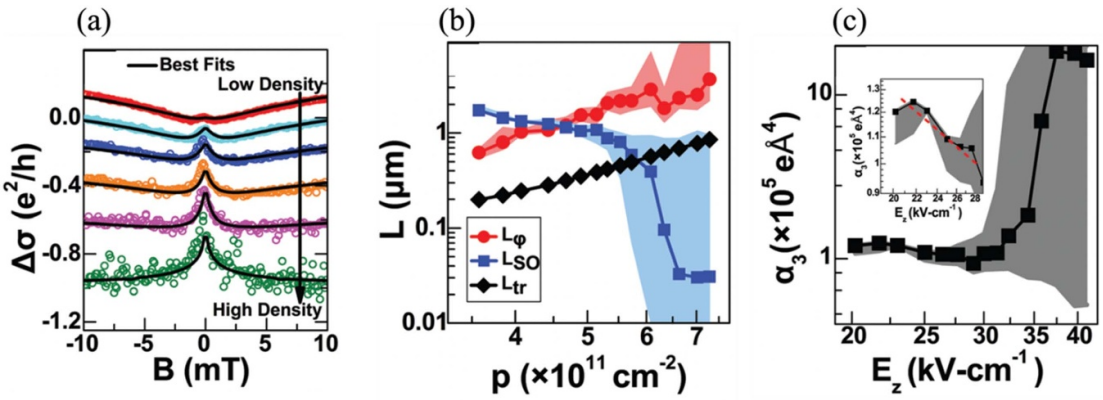

Figure 23. (a) The magneto-conductance at various densities (3.6, 4.1, 4.7, 5.1, 5.5, and 6.6 × 10^{11} cm^{-2}, from top to bottom). The black lines represent fittings by G&G's model. (b) L_ϕ , L_{so}, and L_{tr} vs. hole density (p). (c) α_3 vs. electric field. The inset is the zoom-in at smaller electric fields. Reproduced from [26] with permission from the Royal Society of Chemistry.

effective magnetic field induced by the Rashba effects. Note that in [30], only the k-cubic Rashba term was considered, so the ILP formula reduces to a much simpler form known as Hikami-Larkin-Nagaoka (HLN) formula [123, 124].

With the improvement of the epitaxial growth, in 2018, Chou *et al* reached the spin-ballistic regime in an undoped Ge/$Ge_{0.85}Si_{0.15}$ QW [26]. Their work shows the limitation of both ILP and HLN formula, which are only valid with the following two criteria being satisfied. (1) The system is in a spin-diffusive regime, where the spin precession length ($L_{pre} = v_F \tau_{pre}$, and $\tau_{pre} = 1/\Omega_3$ is the spin precession time) is longer than the mean free path ($L_{tr} = v_F \tau_{tr}$). (2) The applied magnetic field is within the transport characteristic field $B_{tr} = \hbar/2eL_{tr}^2$. This means $L_{tr} < l_B$, where l_B is the magnetic length ($\sqrt{\hbar/eB}$) and the system is in the diffusive regime [125]. In this high-quality sample, the L_{tr} ranges from 0.2 μm to 1 μm, so the B_{tr} ranges from 0.1 mT to 10 mT. Figure 23(a) shows that most of the magneto-transport data were taken out of the range of B_{tr} ($B > 10$ mT or $B < 0.1$ mT), so the authors used a more generalized model proposed by Glazov and Golub (G&G model) [126], which is valid beyond the two criteria. From figure 23(a), those data fit well with the G&G model and τ_ϕ and Ω_3 were able to be extracted from the fittings. Figure 23(b) shows the density dependence of the spin-precession length (Note: the notation of spin-precession length is defined as L_{so} in [26], but L_{pre} in this review.), L_{tr}, and L_ϕ . At a carrier density of ~6 × 10^{11} cm^{-2}, $L_{so} < L_{tr}$ indicates the system enters the spin-ballistic regime. This is essential for the application of spintronics device [120] since the spin states can be maintained and controlled before any scattering events occur to change the spin status. The evolution of α_3 with respect to E_Z is shown in figure 23(c) and the tunability and enhancement of the Rashba SOC by electrical gating were demonstrated for the first time.

Another way to extract the α_3 coefficient is through the beatings of SdH oscillations. Due to the spin splitting, the carrier densities in two spin subbands are different. This results in beatings in the SdH oscillations [25, 113]. Morrison *et al* investigated the beatings in a modulation doped Ge/$Si_{0.2}Ge_{0.8}$ QW [25].

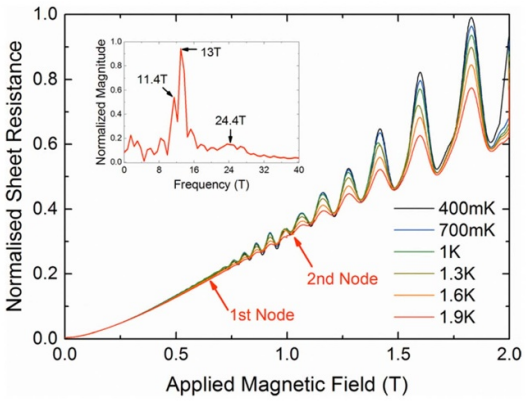

Figure 24. Magneto-resistance vs. magnetic field at different temperatures. The red arrows highlight the beatings in the Shubnikov-de Haas oscillations due to SOC. The inset shows the FFT spectrum up to 1.7 T at 0.4 K. Reprinted from [25], with the permission of AIP Publishing.

The k-cubic Rashba coefficient (β_{so}) is defined as $\beta_{so} = \alpha_3 E_z$ and has the following expression:

$$\beta_{so} = \sqrt{\frac{2}{\pi}} \frac{\hbar^2}{2m^*} \frac{p\,(p_+ - p_-) + \Delta p\,(p_+ + p_-)}{6p^2 + 2\Delta p^2} \tag{6}$$

p is the total hole density, $p_{+(-)} = \sqrt{p \pm \Delta p}$, and Δp is the density difference between the subbands. By analyzing the beatings of SdH patterns, one can extract the subband density and β_{so}. The magneto-transport data are shown in figure 24 and the inset shows the spectrum after performing fast Fourier transform (FFT) steps. The two major peaks at 11.4 T and 13 T correspond to the spin-up and spin-down subbands densities (5.53×10^{11} cm^{-2} and 6.31×10^{11} cm^{-2}), respectively. The small peak at 24.4 T corresponds to the total density. They analyzed the low-field data to extract the effective mass $m^* = 0.095\, m_0$ and used equation (6) to estimate β_{so}. The extracted β_{so} is $1 \pm 0.6 \times 10^{-28}$ eVm^3 with a spin splitting energy of $2\Delta_{so} = 2\beta_{so} k_{\parallel}^3 = 1.4 \pm 0.9$ meV at $k_{\parallel} = 1.93 \times 10^8$ m^{-1}.

We benchmark the Rashba coefficients (β_{so}) extracted by different techniques [24–26, 110, 114], in figure 25. While most of the papers reported the extracted k-cubic term for the Rashba SOC, a recent paper [127] pointed out the possibility to detect the k-linear Rashba term at a very low carrier density. Hendrickx *et al* stated the small k-linear Rashba SOC term offers the theoretical foundation of the fast manipulation of hole spin qubits [15, 16, 28]. However, the contribution of k-linear Rashba term was not observed in the experimental work such as [24, 26]. The reason for the absence of k-linear Rashba term may be the high density in those works. Figure 26 shows the simulation results by using a semi-empirical pseudopotential method (SEPM) to calculate the spin-splitting energy induced by the k-linear or k-cubic Rashba SOC effects [110]. It concluded that the Rashba SOC is dominated by the k-cubic term in the high-density regime where most of the experiment was conducted. However, for QDs applications, since the carrier density is relatively low, the impact of the k-linear Rashba SOC might not be ignored.

6. *G*-factors in Ge-based heterostructures

The g-factor characterizes the Zeeman splitting energy and is important for qubit applications. The g-factor of bulk Ge is expected to be 20.4 [128] while a smaller g-factor is usually observed in a QW structure [35, 128]. Furthermore, there exists the anisotropy of the g-factor. A factor of ~20 times enhancement of the out-of-plane g-factor ($g_{\perp}$) over the in-plane g-factor ($g_{\parallel}$) based on Lüttinger parameters was demonstrated [35]. This can be understood as the results of the quantum confinement and strain in the Ge QW layer [35]. Lu *et al* investigated the anisotropy by measuring $g_{\perp}$ and $g_{\parallel}$ separately at low carrier densities of 1.4×10^{10} cm^{-2}–1.4×10^{11} cm^{-2} [35]. They fabricated an undoped Ge/$Si_{0.2}Ge_{0.8}$ QW structure into an insulated-gate field-effect transistor, so the carrier density can be modulated through gating. Figure 27(a) shows the temperature dependence of magneto-resistance at a hole density of 1.4×10^{11} cm^{-2} near $\nu = 1$. A moving average filter was applied to obtain background signals, and the amplitude (ΔR_{xx}) was extracted by subtracting the background signal (inset of figure 27(a)). The amplitude was then fitted to the temperature dependence of the damping factor $\chi/\sinh(\chi)$, where $\chi = 2\pi^2 k_B T/\Delta$. ($\Delta = \hbar\omega_c$) and this technique is used to extract the effective mass [100]. In this case, at odd ν numbers, the relevant energy gaps are the Zeeman splitting given by $g_{\perp}\mu_B B$ [129]. The $g_{\perp}$ can be extracted through the fitting processes shown in figure 27(b).

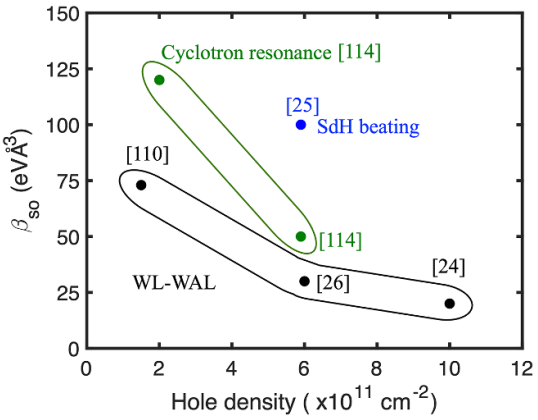

Figure 25. Benchmark of the k-cubic Rashba coefficients ($\beta_{so} = \alpha_3 E_z$) versus hole density. Color code means different techniques. Black: WL/WAL patterns [24, 26, 110], blue: SdH beatings [25], and green: cyclotron resonance [114].

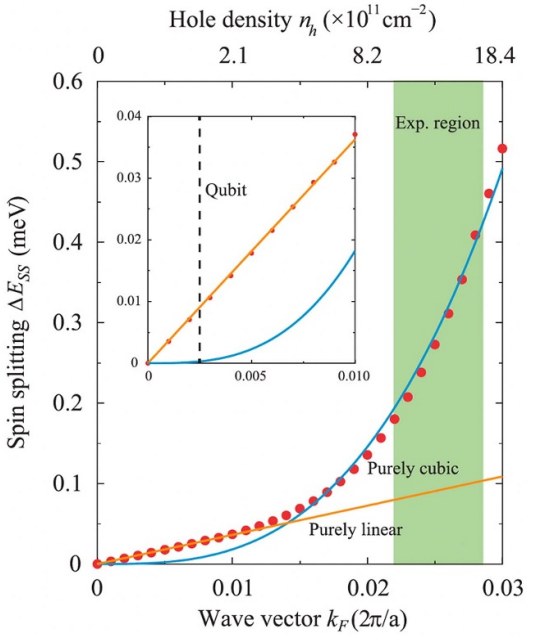

Figure 26. Simulated spin splitting energy versus wavevector along the [100] direction (bottom axis) and hole density (top axis) [110]. The red dots are the calculation results by SEPM. The blue fitting curve is derived by assuming purely k-cubic terms at large k_F, while assuming purely k-linear terms at small k_F to obtain the orange curve. The inset shows the dominant k-linear terms for qubit manipulation. Reprinted figure with permission from [127], Copyright (2022) by the American Physical Society.

In figure 27(c), $g_\perp$ is plotted as a function of hole density. At a given density, $g_\perp$ has a weak dependence on the magnetic field and decreases with the hole density. The largest extracted $g_\perp$ is ∼28 at the lowest density of 1.4×10^{10} cm^{-2}.

To extract the in-plane g-factor, an in-plan magnetic field is applied. Figure 28(a) shows the magneto-resistance (R_{ip}) as a function of the in-plan field at a density of 1.5×10^{10} cm^{-2} at 0.3 K. Only a very weak bump was observed and Lu *et al* subtracted a linear part of the R_{ip} (red dashed line) and plotted in figure 28(b), where an unambiguous maximum appears at the characteristic field (B_{sat}). This indicates that at $B = B_{sat}$, the spin states are fully polarized, and the Fermi energy is equal to the Zeeman splitting: $2\pi\hbar^2 p/m^* = g_\parallel \mu_B B_{sat}$. Using $m^* = 0.9\, m_0$, $g_\parallel$ was estimated and plotted against the carrier density (figure 28(c)). At a density of $\sim 1.5 \times 10^{10}$ cm^{-2}, the extracted $g_\parallel$ is ∼1.3 with an anisotropicity $g_\perp/g_\parallel$ of ∼22.

In 2018, Drichko *et al* [128] investigate $g_\perp$ in a higher density regime, 3.9×10^{11} cm^{-2}–6.2×10^{11} cm^{-2}, for a series of modulation-doped Ge/Si$_x$Ge$_{1-x}$ devices. They used the contactless acoustic method to measure the complex AC conductance ($\sigma \equiv \sigma_1 - i\sigma_2$) and fitted the real part with $\sigma_1 \sim \exp(-\Delta/2kT)$ to extract the activation energy. In their work, the Landau level broadening was also taken into account as $\Gamma_B = C\sqrt{B}$,

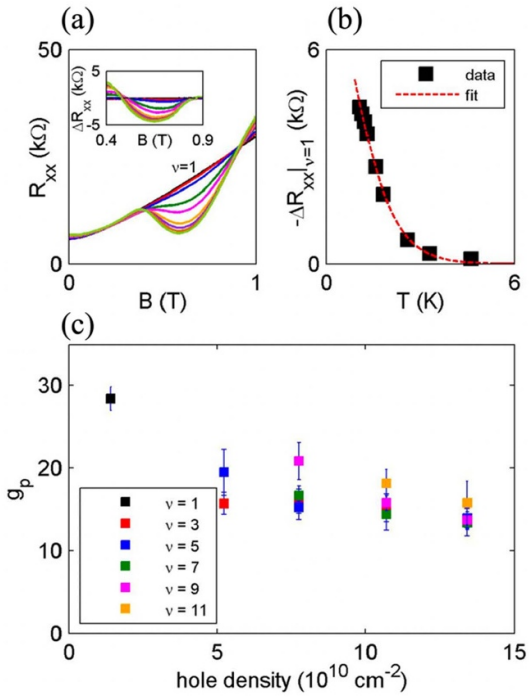

Figure 27. (a) R_{xx} (under an out-of-plane magnetic field) at 1.4×10^{10} cm^{-2} under $T = 4.61$, 3.31, 2.60, 1.82, 1.57, 1.31, 1.22, 1.14, and 1.08 K. The inset shows the amplitudes of SdH oscillations after subtracting background signals. (b) Amplitudes of SdH oscillations vs. temperature. The red dashed line represents the fitting line to the thermal damping factor. (c) Extracted $g_\perp$ (defined as g_p in [35]) versus carrier density. Reprinted from [35], with the permission of AIP Publishing.

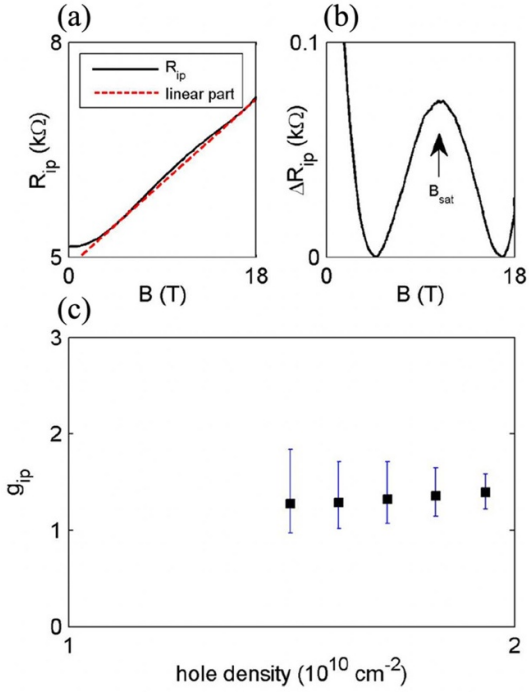

Figure 28. (a) R_{ip} (under an in-plane magnetic field) at a density of 1.5×10^{10} cm^{-2} at 0.3 K. The red dashed line represents the linear component. (b) ΔR_{ip} vs. B. There exists a peak at B_{sat} after subtracting the linear part. B_{sat} indicates full spin saturation at this magnetic field. (c) Extracted $g_{||}$ (defined as g_{ip} in [35]) vs. hole density. Reprinted from [35], with the permission of AIP Publishing.

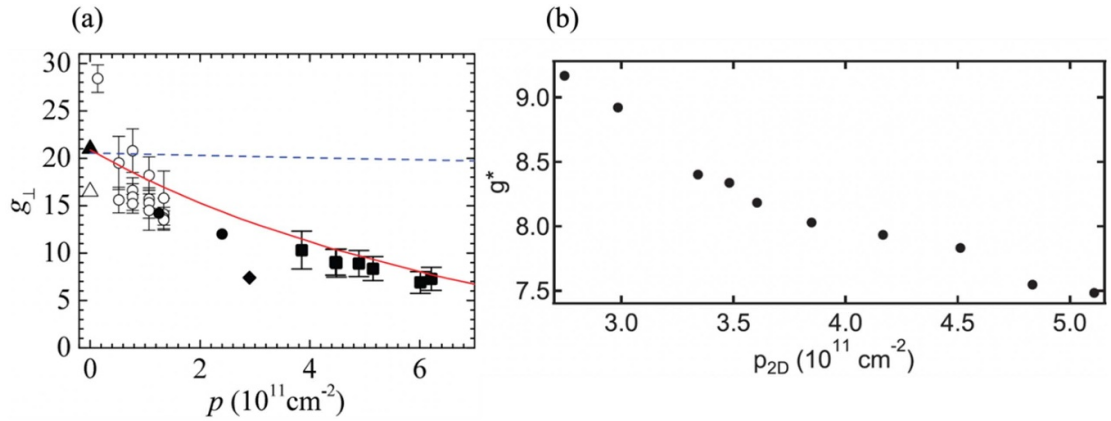

Figure 29. (a) Density dependence of the $g_\perp$ factor. Filled triangles: bulk Ge; filled diamond: [130]; filled circles: [131, 132]; open triangle: [133]; open circles: [35]; filled squares: [128]. The dashed line shows the calculation results based on the $4 \times 4\ \vec{k}\cdot\vec{p}$ Hamiltonian. The solid line shows the results using equation (8) together with a $6 \times 6\ \vec{k}\cdot\vec{p}$ Hamiltonian to include the density dependence of m^*. (b) The estimated $g_\perp$ from the width of FFT spectrum versus carrier density. Reprinted from [128], with the permission of AIP Publishing. [41] John Wiley & Sons. © 2019 The Authors. Published by WILEY-VCH Verlag GmbH & Co. KGaA, Weinheim.

where C is a fitting parameter and B is the applied field. The expression of the energy gap at odd (even) filling factor $\Delta_{\mathrm{odd(even)}}$ is given by:

$$\begin{aligned}\Delta_{\mathrm{odd}} &= g_\perp \mu_B B - \Gamma_B \\ \Delta_{\mathrm{even}} &= \hbar\omega_c - g_\perp \mu_B B - \Gamma_B\end{aligned} \quad . \tag{7}$$

The detailed energy fan diagram can be found in [128]. At a given filling factor minimum, equation (7) is used to derive $g_\perp$ and C assuming $m^* = 0.1\ m_0$. The extracted $g_\perp$ versus the carrier density together with other works [35, 128, 130–133] are illustrated in figure 29(a). For comparison, figure 29(b) shows the results from [41], where $g_\perp$ is estimated from the peak width of the FFT spectrum. The two data sets qualitatively match well, showing a decrease of $g_\perp$ with respect to the carrier density. The author attributed the trend to the non-parabolicity of the valence band due to the mixing of the HH and LH bands. The coupling between the HH states $\left|\frac{3}{2},\pm\frac{3}{2}\right\rangle$ and LH states $\left|\frac{3}{2},\pm\frac{1}{2}\right\rangle$ becomes stronger as $\vec{k}$ increases (equation (2)), so the $g_\perp$ factor becomes a mixture of HH and LH bands. The blue dashed line in figure 29(a) is obtained by using a 4×4 $\vec{k}\cdot\vec{p}$ Hamiltonian, but it cannot explain the data. The author then used an expression between $g_\perp$ and m^*

$$|g_\perp| = \left|2\left[-3\kappa + (\gamma_1 + \gamma_2) - \frac{m_0}{m^*}\right]\right|, \tag{8}$$

where κ, γ_1, and γ_2 are the Lüttinger parameters. By using equation (8) with a $6 \times 6\ \vec{k}\cdot\vec{p}$ Hamiltonian to calculate the dependence of m^*, a good fit is demonstrated (the red curve in figure 29(a)).

7. Summary

While Si-based [14, 134] and Ge-based [15, 16, 135] quantum computing has been demonstrated with high fidelity, the development of group-IV heterostructures requires further improvements for future large-scale qubits. High carrier mobilities more than one million cm^2 (V·s)$^{-1}$ have been demonstrated for Si-based [61] and Ge-based heterostructures [58], but the dominant scattering mechanisms are not yet clear. Future research is required to investigate the ultimate scattering mechanisms to furtherboost the carrier mobility. Surface tunneling, which is a unique property for the undoped heterostructure, is also reviewed. The key physics is the non-equilibrium of charge distributions of two conducting channels in those undoped structures. The carrier mobility in the 2DEG/2DHG layer can be effectively enhanced via the carrier screening from the remote surface conduction channel. The effects of the trapped charge noise were also observed and investigated, but a quantitative model to explain the noise spectrum is still needed to further understand the physics of noise and its impact. While a CMP process can be used to reduce the surface roughness of the heterostructures, the Ge/oxide interface is still much worse than the Si/oxide interface. Further improvement of the oxide/semiconductor interface to reduce the interface trap states will be critical for future success of large-scale qubits with high fidelity. Interested readers can refer to [136] for the Ge/oxide

interface. We also review the previous works on the SOC effect, effective mass, and g-factors in the Ge-based heterostructures. For SOC, two commonly approaches to extracting the k-cubic Rashba coefficients, the pattern of WL/WAL and the beating of SdH oscillations, are discussed. A benchmark of β_{so} including three different experimental techniques are presented. The experimental results can be well explained by the k-cubic Rashba SOC effects and a more negative gate voltage induces more holes and stronger Rashba SOC. However, most of the experiment work focused on the high-density regime, in contrast to the low-density regime where a spin qubit is operated. Although the k-cubic Rashba SOC has been studied extensively, the k-linear term should not be ignored as the density is low. More complete theoretical models or other experimental techniques are needed to fully understand the SOC effects.

We also dive into the hole effective mass in the Ge channel. The hole effective mass in Ge is influenced by the quantum confinement, strained effect, valence-band anisotropy, and non-parabolicity. Both theoretical model and experimental data are reviewed, indicating a reduction of the hole effective mass in a strained-Ge QW or under a smaller carrier density. Finally, we discuss the carrier density dependence and anisotropy of g-factors. A decrease of g-factors with the carrier density is observed for various independent works and can be explained by a $6 \times 6\ \vec{k} \cdot \vec{p}$ Hamiltonian which considers the density dependence of m^*. A large anisotropicity of $g_{\perp}/g_{\parallel}$ ~22 is obtained in a QW structure at a low-density regime and ~ 55 is derived in a QD structure in a single-hole regime. In general, a smaller m^* is desired. The energy difference between subbands is inversely proportional to both m^* and the QD size. To have a well-defined subband separation, a smaller effective mass would allow a larger QD for the same energy difference between any two subbands, easing the nanofabrication complexity. A larger g-factor is desired since a smaller external magnetic field is needed to create the required Zeeman splitting. While the values of m^* and g-factors are well-known for bulk materials, the complexity of the valence band in a 2D structure can introduce anisotropicity for both parameters. While the experimental results of the density dependence of hole effective mass in the Ge/GeSi heterostructure were demonstrated, there is no report for the GeSn/Ge heterostructures, which can be an interesting topic for future study. In summary, the rapid demand on quantum computing have driven the undoped group-IV heterostructures in recent years. Although the challenges are still formidable for Si and Ge qubits, further progress on the material growth and understanding of quantum physics in those heterostructures is expected.

Data availability statement

The data cannot be made publicly available upon publication because they are owned by a third party and the terms of use prevent public distribution. The data that support the findings of this study are available upon reasonable request from the authors.

Acknowledgments

This review has been supported by National Science and Technology Council (NSTC), Taiwan: (grant no: 111-2622-8-002-001-). We gratefully acknowledge the use of the picture (figures 6 and 23) obtained from Nanoscale published by Royal Society of Chemistry.

ORCID iD

Jiun-Yun Li https://orcid.org/0000-0003-4905-9954

References

[1] Shor P W 1994 Algorithms for quantum computation: discrete logarithms and factoring *Proc. 35th Annual Symp. on Foundations of Computer Science* p 124
[2] Arute F *et al* 2020 Hartree-Fock on a superconducting qubit quantum computer *Science* **369** 1084
[3] Monz T, Schindler P, Barreiro J T, Chwalla M, Nigg D, Coish W A and Blatt R 2011 14-qubit entanglement: creation and coherence *Phys. Rev. Lett.* **106** 130506
[4] Dutt M, Childress L, Jiang L, Togan E, Maze J, Jelezko F and Lukin M D 2007 Quantum register based on individual electronic and nuclear spin qubits in diamond *Science* **316** 1312
[5] Petta J R, Johnson A C, Taylor J M, Laird E A, Yacoby A, Lukin M D and Gossard A C 2005 Coherent manipulation of coupled electron spins in semiconductor quantum dots *Science* **309** 2180
[6] Chung Y J, Villegas Rosales K A, Baldwin K W, Madathil P T, West K W, Shayegan M and Pfeiffer L N 2021 Ultra-high-quality two-dimensional electron systems *Nat. Mater.* **20** 632
[7] Kobayashi T, Salfi J, Chua C, van der Heijden J, House M G, Culcer D and Rogge S 2021 Engineering long spin coherence times of spin–orbit qubits in silicon *Nat. Mater.* **20** 38

[8] Schliemann J, Khaetskii A and Loss D 2003 Electron spin dynamics in quantum dots and related nanostructures due to hyperfine interaction with nuclei *J. Phys.* **15** R1809
[9] Chirolli L and Burkard G 2008 Decoherence in solid-state qubits *Adv. Phys.* **57** 225
[10] Tyryshkin A M *et al* 2012 Electron spin coherence exceeding seconds in high-purity silicon *Nat. Mater.* **1** 143
[11] Maune B M, Borselli M G, Huang B, Ladd T D, Deelman P W, Holabird K S and Hunter A T 2012 Coherent singlet-triplet oscillations in a silicon-based double quantum dot *Nature* **481** 344
[12] Huang W, Yang C H, Chan K W, Tanttu T, Hensen B, Leon R C C and Dzurak A S 2019 Fidelity benchmarks for two-qubit gates in silicon *Nature* **569** 532
[13] Yoneda J, Takeda K, Otsuka T, Nakajima T, Delbecq M R, Allison G and Tarucha S 2018 A quantum-dot spin qubit with coherence limited by charge noise and fidelity higher than 99.9% *Nat. Nanotechnol.* **13** 102
[14] Philips S G, Mądzik M T, Amitonov S V, de Snoo S L, Russ M, Kalhor N and Vandersypen L M 2022 Universal control of a six-qubit quantum processor in silicon *Nature* **609** 919
[15] Hendrickx N W, Franke D P, Sammak A, Scappucci G and Veldhorst M 2020 Fast two-qubit logic with holes in germanium *Nature* **577** 487
[16] Hendrickx N W, Lawrie W I, Russ M, van Riggelen F, de Snoo S L, Schouten R N, Sammak A, Scappucci G and Veldhorst M 2021 A four-qubit germanium quantum processor *Nature* **591** 580
[17] Paul D J 2004 Si/SiGe heterostructures: from material and physics to devices and circuits *Semicond. Sci. Technol.* **19** R75
[18] Kasper E and Lyutovich K 2000 *Properties of Silicon Germanium and SiGe: Carbon* (Inspec)
[19] Mooney P M 1996 Strain relaxation and dislocations in SiGe/Si structures *Mater. Sci. Eng.* R **17** 105
[20] Li J Y, Huang C T and Sturm J C 2012 The effect of hydrogen on the surface segregation of phosphorus in epitaxially grown relaxed $Si_{0.7}Ge_{0.3}$ films by rapid thermal chemical vapor deposition *Appl. Phys. Lett.* **101** 142112
[21] Lu T M, Tsui D C, Lee C H and Liu C W 2009 Observation of two-dimensional electron gas in a Si quantum well with mobility of 1.6×10^6 cm^2/Vs *Appl. Phys. Lett.* **94** 182102
[22] Mi X, Hazard T M, Payette C, Wang K, Zajac D M, Cady J V and Petta J R 2015 Magnetotransport studies of mobility limiting mechanisms in undoped Si/SiGe heterostructures *Phys. Rev.* B **92** 035304
[23] Su Y H, Chuang Y, Liu C Y, Li J Y and Lu T M 2017 Effects of surface tunneling of two-dimensional hole gases in undoped Ge/GeSi heterostructures *Phys. Rev. Mater.* **1** 044601
[24] Moriya R *et al* 2014 Cubic Rashba spin-orbit interaction of a two-dimensional hole gas in a strained-Ge/SiGe quantum well *Phys. Rev. Lett.* **113** 086601
[25] Morrison C, Wiśniewski P, Rhead S D, Foronda J, Leadley D R and Myronov M 2014 Observation of Rashba zero-field spin splitting in a strained germanium 2D hole gas *Appl. Phys. Lett.* **105** 182401
[26] Chou C T, Jacobson N T, Moussa J E, Baczewski A D, Chuang Y, Liu C Y, Li J Y and Lu T M 2018 Weak anti-localization of two-dimensional holes in germanium beyond the diffusive regime *Nanoscale* **10** 20599
[27] Morrison C and Myronov M 2016 Strained germanium for applications in spintronics *Phys. Status Solidi* a **213** 2809
[28] Hendrickx N W *et al* 2018 Gate-controlled quantum dots and superconductivity in planar germanium *Nat. Commun.* **9** 2835
[29] Watzinger H, Kukučka J, Vukušić L, Gao F, Wang T, Schäffler F, Zhang J J and Katsaros G 2018 A germanium hole spin qubit *Nat. Commun.* **9** 3902
[30] Tai C T, Chiu P Y, Liu C Y, Kao H S, Harris C T, Lu T M, Hsieh C T, Chang S W and Li J Y 2021 Strain effects on rashba spin-orbit coupling of 2D hole gases in GeSn/Ge heterostructures *Adv. Mater.* **33** 2007862
[31] Liu C Y, Tien K Y, Chiu P Y, Wu Y J, Chuang Y, Kao H S and Li J Y 2022 Room-temperature negative differential resistance and high tunneling current density in GeSn Esaki diodes *Adv. Mater.* **34** 2203888
[32] Liu T H, Chiu P Y, Chuang Y, Liu C Y, Shen C H, Luo G L and Li J Y 2018 High-mobility GeSn n-channel MOSFETs by low-temperature chemical vapor deposition and microwave annealing *IEEE Electron Device Lett.* **39** 468
[33] Chuang Y, Liu C Y, Luo G L and Li J Y 2020 Electron mobility enhancement in GeSn n-channel MOSFETs by tensile strain *IEEE Electron Device Lett.* **42** 10
[34] Lodari M, Tosato A, Sabbagh D, Schubert M A, Capellini G, Sammak A, Veldhorst M and Scappucci G 2019 Light effective hole mass in undoped Ge/SiGe quantum wells *Phys. Rev.* B **100** 041304
[35] Lu T M, Harris C T, Huang S H, Chuang Y, Li J Y and Liu C W 2017 Effective g factor of low-density two-dimensional holes in a Ge quantum well *Appl. Phys. Lett.* **111** 102108
[36] Sawano K, Toyama K, Masutomi R, Okamoto T, Usami N, Arimoto K, Nakagawa K and Shiraki Y 2009 Strain dependence of hole effective mass and scattering mechanism in strained Ge channel structures *Appl. Phys. Lett.* **95** 122109
[37] Terrazos L A *et al* 2021 Theory of hole-spin qubits in strained germanium quantum dots *Phys. Rev.* B **103** 125201
[38] Vukušić L, Kukucka J, Watzinger H, Milem J M, Schäffler F and Katsaros G 2018 Single-shot readout of hole spins in Ge *Nano Lett.* **18** 7141
[39] Maurand R *et al* 2016 A CMOS silicon spin qubit *Nat. Commun.* **7** 13575
[40] Hwang J C C, Yang C H, Veldhorst M, Hendrickx N, Fogarty M A, Huang W, Hudson F E, Morello A and Dzurak A S 2017 Impact of g-factors and valleys on spin qubits in a silicon double quantum dot *Phys. Rev.* B **96** 045302
[41] Sammak A *et al* 2019 Shallow and undoped germanium quantum wells: a playground for spin and hybrid quantum technology *Adv. Funct. Mater.* **29** 1807613
[42] Jirovec D *et al* 2021 A singlet-triplet hole spin qubit in planar Ge *Nat. Mater.* **20** 1106
[43] Scappucci G, Kloeffel C, Zwanenburg F A, Loss D, Myronov M, Zhang J-J, De Franceschi S, Katsaros G and Veldhorst M 2021 The germanium quantum information route *Nat. Rev. Mater.* **6** 926
[44] Fang Y, Philippopoulos P, Culcer D, Coish W A and Chesi S 2023 Recent advances in hole-spin qubits *Mater. Quantum Technol.* **3** 012003
[45] Umansky V, De-Picciotto R and Heiblum M 1997 Extremely high-mobility two dimensional electron gas: evaluation of scattering mechanisms *Appl. Phys. Lett.* **71** 683
[46] Ismail K, Meyerson B S and Wang P J 1991 High electron mobility in modulation-doped Si/SiGe *Appl. Phys. Lett.* **58** 2117
[47] Medford J, Beil J, Taylor J M, Rashba E I, Lu H, Gossard A C and Marcus C M 2013 Quantum-dot-based resonant exchange qubit *Phys. Rev. Lett.* **111** 050501
[48] Nichol J M, Orona L A, Harvey S P, Fallahi S, Gardner G C, Manfra M J and Yacoby A 2017 High-fidelity entangling gate for double-quantum-dot spin qubits *npj Quantum Inf.* **3** 3

[49] Studenikin S *et al* 2019 Electrically tunable effective g-factor of a single hole in a lateral GaAs/AlGaAs quantum dot *Commun. Phys.* **2** 15
[50] Chang L T *et al* 2016 Electrical detection of spin transport in Si two-dimensional electron gas systems *Nanotechnology* **27** 365701
[51] Assali L V C, Petrilli H M, Capaz R B, Koiller B, Hu X and Sarma S D 2011 Hyperfine interactions in silicon quantum dots *Phys. Rev.* B **83** 165301
[52] Lai K, Ye P D, Pan W, Tsui D C, Lyon S A, Mühlberger M and Schäffler F 2005 Modulation of the high mobility two-dimensional electrons in Si/ Si Ge using atomic-layer-deposited gate dielectric *Appl. Phys. Lett.* **87** 142103
[53] Nixon J A and Davies J H 1990 Potential fluctuations in heterostructure devices *Phys. Rev.* B **41** 7929
[54] Abstreiter G, Brugger H, Wolf T, Jorke H and Herzog H J 1985 Strain-induced two-dimensional electron gas in selectively doped Si/Si_xGe_{1-x} superlattices *Phys. Rev. Lett.* **54** 2441
[55] Sugii N, Nakagawa K, Kimura Y, Yamaguchi S and Miyao M 1998 High electron mobility in strained Si channel of heterostructure with abrupt interface *Semicond. Sci. Technol.* **13** A140
[56] Degli Esposti D, Paquelet Wuetz B, Fezzi V, Lodari M, Sammak A and Scappucci G 2022 Wafer-scale low-disorder 2DEG in ^{28}Si/SiGe without an epitaxial Si cap *Appl. Phys. Lett.* **120** 184003
[57] Dobbie A, Myronov M, Morris R J H, Hassan A H A, Prest M J, Shah V A and Leadley D R 2012 Ultra-high hole mobility exceeding one million in a strained germanium quantum well *Appl. Phys. Lett.* **101** 172108
[58] Lodari M, Kong O, Rendell M, Tosato A, Sammak A, Veldhorst M and Scappucci G 2022 Lightly strained germanium quantum wells with hole mobility exceeding one million *Appl. Phys. Lett.* **120** 122104
[59] Li J Y, Huang C T, Rokhinson L P and Sturm J C 2013 Extremely low electron density in a modulation-doped Si/SiGe two-dimensional electron gases by effective Schottky gating *ECS Trans.* **50** 145
[60] Li J Y, Huang C T, Rokhinson L P and Sturm J C 2013 Extremely high electron mobility in isotopically-enriched ^{28}Si two-dimensional electron gases grown by chemical vapor deposition *Appl. Phys. Lett.* **103** 162105
[61] Melnikov M Y, Shashkin A A, Dolgopolov V T, Huang S H, Liu C W and Kravchenko S V 2015 Ultra-high mobility two-dimensional electron gas in a SiGe/Si/SiGe quantum well *Appl. Phys. Lett.* **106** 092102
[62] Huang S H, Lu T M, Lu S C, Lee C H, Liu C W and Tsui D C 2012 Mobility enhancement of strained Si by optimized SiGe/Si/SiGe structures *Appl. Phys. Lett.* **101** 042111
[63] Monroe D, Xie Y H, Fitzgerald E A, Silverman P J and Watson G P 1993 Comparison of mobility-limiting mechanisms in high-mobility $Si_{1-x}Ge_x$ heterostructures *J. Vac. Sci. Technol.* B **11** 1731
[64] Godbey D J and Ancona M G 1992 Ge profile from the growth of SiGe buried layers by molecular beam epitaxy *Appl. Phys. Lett.* **61** 2217
[65] Laroche D, Huang S H, Nielsen E, Chuang Y, Li J Y, Liu C W and Lu T M 2015 Scattering mechanisms in shallow undoped Si/SiGe quantum wells *AIP Adv.* **5** 107106
[66] Gold A 1988 Scattering time and single-particle relaxation time in a disordered two-dimensional electron gas *Phys. Rev.* B **38** 10798
[67] Basaran E, Kubiak R A, Whall T E and Parker E H C 1994 Very high two-dimensional hole gas mobilities in strained silicon germanium *Appl. Phys. Lett.* **64** 3470
[68] Fischettia M V and Laux S E 1996 Band structure, deformation potentials, and carrier mobility in strained Si, Ge, and SiGe alloys *J. Appl. Phys.* **80** 2234
[69] Myronov M, Sawano K, Shiraki Y, Mouri T and Itoh K M 2008 Observation of high mobility 2DHG with very high hole density in the modulation doped strained Ge quantum well at room temperature *Physica* E **40** 1935
[70] Rössner B, Chrastina D, Isella G and Von Känel H 2004 Scattering mechanisms in high-mobility strained Ge channels *Appl. Phys. Lett.* **84** 3058
[71] Shah V A, Dobbie A, Myronov M, Fulgoni D J F, Nash L J and Leadley D R 2008 Reverse graded relaxed buffers for high Ge content SiGe virtual substrates *Appl. Phys. Lett.* **93** 192103
[72] Luan H C, Lim D R, Lee K K, Chen K M, Sandland J G, Wada K and Kimerling L C 1999 High-quality Ge epilayers on Si with low threading-dislocation densities *Appl. Phys. Lett.* **75** 2909
[73] Dimoulas A, Tsipas P, Sotiropoulos A and Evangelou E K 2006 Fermi-level pinning and charge neutrality level in germanium *Appl. Phys. Lett.* **89** 252110
[74] Chiu P Y, Lidsky D, Chuang Y, Su Y H, Li J Y, Harris C T and Lu T M 2020 Post-growth modulation doping by ion implantation *Appl. Phys. Lett.* **117** 263502
[75] Laroche D, Huang S H, Chuang Y, Li J Y, Liu C W and Lu T M 2016 Magneto-transport analysis of an ultra-low-density two-dimensional hole gas in an undoped strained Ge/SiGe heterostructure *Appl. Phys. Lett.* **108** 233504
[76] Chuang P *et al* 2015 All-electric all-semiconductor spin field-effect transistors *Nat. Nanotechnol.* **10** 35
[77] Huang B, Monsma D J and Appelbaum I 2007 Experimental realization of a silicon spin field-effect transistor *Appl. Phys. Lett.* **91** 072501
[78] Tang J *et al* 2013 Electrical spin injection and detection in Mn_5Ge_3/Ge/Mn_5Ge_3 nanowire transistors *Nano Lett.* **13** 4036
[79] Mehrotra S R, Paul A and Klimeck G 2011 Atomistic approach to alloy scattering in $Si_{1-x}Ge_x$ *Appl. Phys. Lett.* **98** 173503
[80] Gold A 2010 Mobility and metal–insulator transition of the two-dimensional electron gas in SiGe/Si/SiGe quantum wells *J. Appl. Phys.* **108** 063710
[81] Hendrickx N W, Massai L, Mergenthaler M, Schupp F, Paredes S, Bedell S W, Salis G and Fuhrer A 2023 Sweet-spot operation of a germanium hole spin qubit with highly anisotropic noise sensitivity (arXiv:2305.13150)
[82] Massai L *et al* 2023 Impact of interface traps on charge noise, mobility and percolation density in Ge/SiGe heterostructures (arXiv:2310.05902)
[83] Lu T M, Lee C H, Huang S H, Tsui D C and Liu C W 2011 Upper limit of two-dimensional electron density in enhancement-mode Si/SiGe heterostructure field-effect transistors *Appl. Phys. Lett.* **99** 153510
[84] Huang C T, Li J Y, Chou K S and Sturm J C 2014 Screening of remote charge scattering sites from the oxide/silicon interface of strained Si two-dimensional electron gases by an intermediate tunable shielding electron layer *Appl. Phys. Lett.* **104** 243510
[85] Su Y H, Chou K Y, Chuang Y, Lu T M and Li J Y 2019 Electron mobility enhancement in an undoped Si/SiGe heterostructure by remote carrier screening *J. Appl. Phys.* **125** 235705
[86] Chou K Y, Hsu N W, Su Y H, Chou C T, Chiu P Y, Chuang Y and Li J Y 2018 Temperature dependence of DC transport characteristics for a two-dimensional electron gas in an undoped Si/SiGe heterostructure *Appl. Phys. Lett.* **112** 083502
[87] Davies J H 1997 *The Physics of Low-dimensional Semiconductors: An Introduction* (Cambridge University Press)

[88] Sabbagh D, Thomas N, Torres J, Pillarisetty R, Amin P, George H C and Scappucci G 2019 Quantum transport properties of industrial ^{28}Si/^{28}SiO2 *Phys. Rev. Appl.* **12** 014013
[89] Hou W C, Hsu N W, Wang T M, Liu C Y, Kao H S, Chen M J and Li J Y 2022 Cryogenic Si/SiGe heterostructure flash memory devices *ACS Appl. Electron. Mater.* **4** 2879
[90] Hsu N W, Hou W C, Chen Y Y, Wu Y J, Kao H S, Harris C T and Li J Y 2022 Temperature dependence of charge distributions and carrier mobility in an undoped Si/SiGe heterostructure *IEEE Trans. Electron Devices* **69** 482
[91] Ashcroft N W and Mermin N D 1976 *Solid State Physics* (Saunders College)
[92] Wong I H, Chen Y T, Huang S H, Tu W H, Chen Y S and Liu C W 2015 Junctionless gate-all-around pFETs using in-situ boron-doped Ge channel on Si *IEEE Trans. Nanotechnol.* **14** 878
[93] Sugahara S and Nitta J 2010 Spin-transistor electronics: an overview and outlook *Proc. IEEE* **98** 2124
[94] Luttinger J M and Kohn W 1955 Motion of electrons and holes in perturbed periodic fields *Phys. Rev.* **97** 869
[95] Luttinger J M 1956 Quantum theory of cyclotron resonance in semiconductors: general theory *Phys. Rev.* **102** 1030
[96] Wang C-A, Scappucci G, Veldhorst M and Russ M 2022 Modelling of planar germanium hole qubits in electric and magnetic fields (arXiv:2208.04795)
[97] Bir G L, Pikus G E and Louvish D 1974 *Symmetry and Strain-induced Effects in Semiconductors* (Wiley)
[98] Chuang S L 2009 *Physics of Photonic Devices* 2nd edn (John Wiley)
[99] Wortman J J and Evans R A 1965 Young's modulus, shear modulus, and Poisson's ratio in silicon and germanium *J. Appl. Phys.* **36** 153
[100] Berkutov I B, Andrievskiĭ V V, Komnik Y F, Mironov O A, Mironov M and Leadley D R 2009 Shubnikov-de Haas oscillations of the conductivity of a two-dimensional gas in quantum wells based on germanium and silicon. Determination of the effective mass and g factor *Low Temp. Phys.* **35** 141–5
[101] Komnik Y F, Berkutov I B, Andrievskiĭ V V, Mironov O A, Myronov M and Leadley D R 2006 Features of the Shubnikov–de Haas oscillations of the conductivity of a high-mobility two-dimensional hole gas in a SiGe/Ge/SiGe quantum well *Low Temp. Phys.* **32** 82
[102] Ridley B K 2009 *Electrons and Phonons in Semiconductor Multilayers* (Cambridge University Press)
[103] Rößner B, Isella G and Känel H V 2003 Effective mass in remotely doped Ge quantum wells *Appl. Phys. Lett.* **82** 754
[104] Irisawa T, Myronov M, Mironov O A, Parker E H C, Nakagawa K, Murata M, Koh S and Shiraki Y 2003 Hole density dependence of effective mass, mobility and transport time in strained Ge channel modulation-doped heterostructures *Appl. Phys. Lett.* **82** 1425
[105] Foreman B A 1994 Analytic model for the valence-band structure of a strained quantum well *Phys. Rev.* B **49** 1757
[106] Winkler R 2003 *Spin-orbit Coupling Effects in Two-Dimensional Electron and Hole Systems* (Springer)
[107] Dresselhaus G 1955 Spin-orbit coupling effects in zinc blende structures *Phys. Rev.* **100** 580
[108] Bychkov Y A and Rashba E I 1984 Oscillatory effects and the magnetic susceptibility of carriers in inversion layers *J. Phys. C: Solid State Phys.* **17** 6039
[109] Nakamura H, Koga T and Kimura T 2012 Experimental evidence of cubic Rashba effect in an inversion-symmetric oxide *Phys. Rev. Lett.* **108** 206601
[110] Mizokuchi R, Torresani P, Maurand R, Zeng Z, Niquet Y M, Myronov M and De Franceschi S 2017 Hole weak anti-localization in a strained-Ge surface quantum well *Appl. Phys. Lett.* **111** 063102
[111] Newton P J, Mansell R, Holmes S N, Myronov M and Barnes C H W 2017 Weak localization and weak antilocalization in doped germanium epilayers *Appl. Phys. Lett.* **110** 062101
[112] Foronda J, Morrison C, Halpin J E, Rhead S D and Myronov M 2014 Weak antilocalization of high mobility holes in a strained Germanium quantum well heterostructure *J. Phys.* **27** 022201
[113] Morrison C, Foronda J, Wiśniewski P, Rhead S D, Leadley D R and Myronov M 2016 Evidence of strong spin–orbit interaction in strained epitaxial germanium *Thin Solid Films* **602** 84
[114] Failla M, Myronov M, Morrison C, Leadley D R and Lloyd-Hughes J 2015 Narrow heavy-hole cyclotron resonances split by the cubic Rashba spin-orbit interaction in strained germanium quantum wells *Phys. Rev.* B **92** 045303
[115] Rammer J 1998 *Quantum Transport Theory* (Perseus Books)
[116] Winkler R, Culcer D, Papadakis S J, Habib B and Shayegan M 2008 Spin orientation of holes in quantum wells *Semicond. Sci. Technol.* **23** 114017
[117] Iordanskii S V, Lyanda-Geller Y B and Pikus G E 1994 Weak localization in quantum wells with spin-orbit interaction *JETP Lett.* **60** 199
[118] Minkov G M, Sherstobitov A A, Germanenko A V, Rut O E, Larionova V A and Zvonkov B N 2005 Antilocalization and spin-orbit coupling in the hole gas in strained $Ga_xAs/In_xGa_{1-x}As/GaAs$ quantum well heterostructures *Phys. Rev. B* **71** 165312
[119] Liang H, Cheng L, Wei L, Luo Z, Yu G, Zeng C and Zhang Z 2015 Nonmonotonically tunable Rashba spin-orbit coupling by multiple-band filling control in $SrTiO_3$-based interfacial d-electron gases *Phys. Rev.* B **92** 075309
[120] Žutić I, Fabian J and Sarma S D 2004 Spintronics: fundamentals and applications *Rev. Mod. Phys.* **76** 323
[121] Elliott R J 1954 Theory of the effect of spin-orbit coupling on magnetic resonance in some semiconductors *Phys. Rev.* **96** 266
[122] Yafet Y 1983 Conduction electron spin relaxation in the superconducting state *Phys. Lett.* A **98** 287
[123] Hikami S, Larkin A I and Nagaoka Y 1980 Spin-orbit interaction and magnetoresistance in the two dimensional random system *Prog. Theor. Phys.* **63** 707
[124] Dresselhaus P D, Papavassiliou C M A, Wheeler R G and Sacks R N 1992 Observation of spin precession in GaAs inversion layers using antilocalization *Phys. Rev. Lett.* **68** 106
[125] Golub L E 2005 Weak antilocalization in high-mobility two-dimensional systems *Phys. Rev.* B **71** 235310
[126] Glazov M M and Golub L E 2006 Nondiffusive weak localization in two-dimensional systems with spin-orbit splitting of the spectrum *Semiconductors* **40** 1209
[127] Xiong J X, Liu Y, Guan S, Luo J W and Li S S 2022 Why experiments fail to detect the finite linear Rashba spin-orbit coupling of two-dimensional holes in semiconductor quantum wells: the case of Ge/SiGe quantum wells *Phys. Rev.* B **106** 155421
[128] Drichko I L, Dmitriev A A, Malysh V A, Smirnov I Y, von Känel H, Kummer M, Chrastina D and Isella G 2018 Effective g factor of 2D holes in strained Ge quantum wells *J. Appl. Phys.* **123** 165703
[129] Lu T M, Tracy L A, Laroche D, Huang S H, Chuang Y, Su Y H, Li J Y and Liu C W 2017 Density-controlled quantum Hall ferromagnetic transition in a two-dimensional hole system *Sci. Rep.* **7** 2468
[130] Shi Q, Zudov M A, Morrison C and Myronov M 2015 Spinless composite fermions in an ultrahigh-quality strained Ge quantum well *Phys. Rev.* B **91** 241303

[131] Arapov Y G, Harus G I, Shelushinina N G, Yakunin M V, Neverov V N, Kuznetsov O A, Ponomarenko L and De Visser A 2004 Nonmonotonic temperature dependence of the resistivity of p-Ge/$Ge_{1-x}Si_x$ in the region of the metal–insulator transition *Low Temp. Phys.* **30** 867
[132] Arapov Y G, Gudina S V, Karskanov I V, Neverov V N, Harus G I and Shelushinina N G 2007 Contributions of the electron–electron interaction and weak localization to the conductance of p-Ge/$Ge_{1-x}Si_x$ heterostructures *Low Temp. Phys.* **33** 160
[133] Nenashev A V, Dvurechenskii A V and Zinovieva A F 2003 Wave functions and g factor of holes in Ge/Si quantum dots *Phys. Rev.* B **67** 205301
[134] Mills A R, Guinn C R, Feldman M M, Sigillito A J, Gullans M J, Rakher M T, Kerckhoff J, Jackson C A C and Petta J R 2022 High-fidelity state preparation, quantum control, and readout of an isotopically enriched silicon spin qubit *Phys. Rev. Appl.* **18** 064028
[135] Borsoi F, Hendrickx N W, John V, Meyer M, Motz S, van Riggelen F, Sammak A, de Snoo S L, Scappucci G and Veldhorst M 2023 Shared control of a 16 semiconductor quantum dot crossbar array *Nat. Nanotechnol.* **18** 1
[136] Kamata Y 2008 High-k/Ge MOSFETs for future nanoelectronics *Mater. Today* **11** 30